JGR Atmospheres

RESEARCH ARTICLE
10.1029/2020JD032463

Atmospheric Drivers of Melt on Larsen C Ice Shelf: Surface Energy Budget Regimes and the Impact of Foehn

Andrew D. Elvidge[1], Peter Kuipers Munneke[2], John C. King[3], Ian A. Renfrew[1], and Ella Gilbert[1,3]

[1]School of Environmental Sciences, University of East Anglia, Norwich, UK, [2]Institute for Marine and Atmospheric Research Utrecht, Utrecht, The Netherlands, [3]British Antarctic Survey, Cambridge, UK

Key Points:
- Spatial variability and maxima in Larsen C melt are chiefly due to foehn-driven sensible heating, though most melt is due to solar radiation
- Low static stability reverses the usual positive correlation between melt and foehn wind speed, explaining conflicting results in previous studies
- A high-resolution atmospheric model capably reproduces melt patterns across Larsen C but has notable biases in the surface radiative fluxes

Correspondence to:
A. D. Elvidge,
a.elvidge@uea.ac.uk

Citation:
Elvidge, A. D., Kuipers Munneke, P., King, J. C., Renfrew, I. A., & Gilbert, E. (2020). Atmospheric drivers of melt on Larsen C Ice Shelf: Surface energy budget regimes and the impact of foehn. *Journal of Geophysical Research: Atmospheres*, *125*, e2020JD032463. https://doi.org/10.1029/2020JD032463

Received 17 JAN 2020
Accepted 20 MAY 2020
Accepted article online 22 MAY 2020

Abstract Recent ice shelf retreat on the east coast of the Antarctic Peninsula has been principally attributed to atmospherically driven melt. However, previous studies on the largest of these ice shelves—Larsen C—have struggled to reconcile atmospheric forcing with observed melt. This study provides the first comprehensive quantification and explanation of the atmospheric drivers of melt across Larsen C, using 31-months' worth of observations from Cabinet Inlet, a 6-month, high-resolution atmospheric model simulation and a novel approach to ascertain the surface energy budget (SEB) regime. The dominant meteorological controls on melt are shown to be the occurrence, strength, and warmth of mountain winds called foehn. At Cabinet Inlet, foehn occurs 15% of the time and causes 45% of melt. The primary effect of foehn on the SEB is elevated turbulent heat fluxes. Under typical, warm foehn conditions, this means elevated surface heating and melting, the intensity of which increases as foehn wind speed increases. Less commonly—due to cooler-than-normal foehn winds and/or radiatively warmed ice—the relationship between wind speed and net surface heat flux reverses. This explains the seemingly contradictory results of previous studies. In the model, spatial variability in cumulative melt across Larsen C is largely explained by foehn, with melt maxima in inlets reflecting maxima in foehn wind strength. However, most accumulated melt (58%) occurs due to solar radiation in the absence of foehn. A broad north-south gradient in melt is explained by the combined influence of foehn and non-foehn conditions.

Plain Language Summary The recent rapid retreat and collapse of ice shelves on the east coast of the Antarctic Peninsula is known to be primarily a result of enhanced surface melt due to climate warming and changing atmospheric circulation patterns. However, previous studies have struggled to reconcile observed melt patterns with meteorological conditions. Here we provide the first quantification and explanation of the atmospheric drivers of melt across Larsen C, the largest ice shelf on the Antarctic Peninsula. We find that variability in melt across Larsen C is primarily governed by mountain winds known as foehn, with melt maxima in ice shelf inlets coinciding with the strongest foehn winds. Foehn air is usually much warmer than the ice below, resulting in elevated heating and melting of the ice, the intensity of which increases with increasing wind speed. However, in rare cases where the foehn air is not significantly warmer than the ice, the relationship between melt and foehn wind speed reverses, which explains the seemingly contradictory results of previous studies. While foehn causes the highest melt rates, non-foehn-driven melt is more common and, via summertime solar heating, is responsible for most of the accumulation of melt across the ice shelf as a whole.

1. Introduction

The retreat and collapse of ice shelves on the Antarctic Peninsula (AP) over recent decades has been principally attributed to surface melt due to atmospheric warming (Cook & Vaughan, 2010; Holland et al., 2011; Leeson et al., 2017; Scambos et al., 2000; Valisuo et al., 2014; Van den Broeke, 2005). Changing southern hemispheric circulation patterns have led to increased warm air advection into the region via a strengthening of the prevailing circumpolar westerly winds and also to an increase in the frequency and strength of low-level warming events to the east of the AP caused by mountain-generated local winds known as foehn (Cape et al., 2015; Marshall et al., 2006; Orr et al., 2008; Van Lipzig et al., 2008). This foehn warming effect has led to asymmetrical warming across the AP in summer, the warming rate to the east being considerably greater than that to the west (3 times as great at the northern tip; Marshall et al., 2006). The Stretching along the Peninsula's east coast, the Larsen Ice Shelf, first mapped in 1893 (Larsen, 1894), is composed of four

distinctly evolving components (Vaughan & Doake, 1996). The northernmost two components—A and B—disintegrated in 1995 and 2002, respectively. The disintegration of Larsen B was immediately preceded by extensive meltwater ponding and high levels of ice densification (from the refreezing of meltwater in the firn layer), a known precursor of ice shelf collapse (Holland et al., 2011; Kuipers Munneke et al., 2014). Immediately to the south, Larsen C is the largest ice shelf on the AP and is presently intersected by the mean annual (near-surface level) −9°C isotherm; loosely approximating the upper limit for ice shelf viability (Morris & Vaughan, 2003). Densification in the northwest embayments, or inlets, of Larsen C is approaching those levels observed in Larsen B immediately prior to its collapse (Holland et al., 2011; Hubbard et al., 2016).

Foehn is a downslope wind in the lee of a mountain that is accelerated, warmed, and dried as a result of the orographic disturbance on the prevailing flow (Elvidge & Renfrew, 2016). It is an intrinsic feature of mountain gravity waves, and can also be generated or strengthened by cross-mountain pressure gradients driving "gap flows" through elevated mountain passes (Elvidge et al., 2015; Mayr et al., 2007; Zängl, 2003). The warmth of foehn, combined with the accompanying dry, cloud-free conditions (the foehn cloud-clearance effect), makes it a potent agent for ice and snow melt (Cape et al., 2015; Elvidge et al., 2016; Hayashi et al., 2005). Over Larsen C, a series of case study investigations using observations supported by relatively high resolution simulations have demonstrated the capacity for foehn to penetrate down to the surface in the immediate lee of the mountains and in certain cases (when the mountain flow regime is relatively linear) to extend across the entire ice shelf (e.g., Elvidge et al., 2016, 2015; Grosvenor et al., 2014; King et al., 2008; Turton et al., 2018). Foehn is typically channeled into the inlets, forming foehn jets, between which sheltered regions experiencing weaker foehn winds ("wake" regions) are found (Elvidge et al., 2015). Several studies have demonstrated that foehn enhances melt rates over Larsen C, via increased downward surface fluxes of shortwave radiation and sensible heat (Datta et al., 2019; Elvidge et al., 2016; King et al., 2017; Kuipers Munneke et al., 2018, 2012). Using data from satellite observations and a regional climate model, Datta et al. (2019) have attributed enhanced late summer-season meltwater percolation depths and snow densification during recent years to foehn. It has also been shown that the collapse of Larsen B was coincident with a summer of anomalously strong foehn warming (Cape et al., 2015).

Luckman et al. (2014) presented satellite observations of climatological melt distributions over Larsen C, the key features of which are corroborated by other studies (e.g., Ashmore et al., 2017; Barrand et al., 2013; Bevan et al., 2018; Holland et al., 2011; Tedesco, 2009). They revealed that the distribution in observed melt broadly matches patterns in near-surface wind speed and air temperature in case study simulations of foehn; patterns which have also been seen in composite foehn conditions from a multidecadal model simulation (Wiesenekker et al., 2018). More specifically, elevated melt rates in a narrow band running along the AP's east coast at the foot of the mountains mirrors the diminishing impact of foehn on leeside temperatures with distance downwind of the AP (Elvidge et al., 2016), while melt rate maxima in inlets are colocated with maxima in foehn wind speed (Elvidge et al., 2015). A broad north to south gradient in melt reflects both the annual mean gradient in solar irradiance at the top of the atmosphere and the north-south gradient in the strength of the background circumpolar westerly winds which drive foehn in this region (Marshall et al., 2006). It also corresponds with the prevailing foehn wind direction across Larsen C being broadly northwesterly (Datta et al., 2019; Turton et al., 2018).

Given these correlations, a reasonable hypothesis is that foehn plays a governing role in climatological melt patterns over Larsen C. However, the supporting evidence for this hypothesis is conflicted:

- In model data spanning one melt season, King et al. (2017) found that the impact of foehn on Larsen C's surface energy budget (SEB) was generally small and that, besides enhanced melt toward the far north of the ice shelf, the spatial pattern of foehn-driven melt bore little resemblance to satellite observations. However, noting the absence of foehn jets in their meteorological analysis data, they call into question the validity of these results on account of model shortcomings, including a limited resolution.
- Beyond the cloud-clearance effect, the impact of foehn is governed by a balance between downward fluxes of sensible heat (SH) due to the relative warmth of the foehn air and upward fluxes of latent heat (LH) due to sublimation. The available evidence demonstrates significant seasonal, diurnal, and spatial variability in this balance, meaning the net effect is not necessarily surface warming. During wintertime and

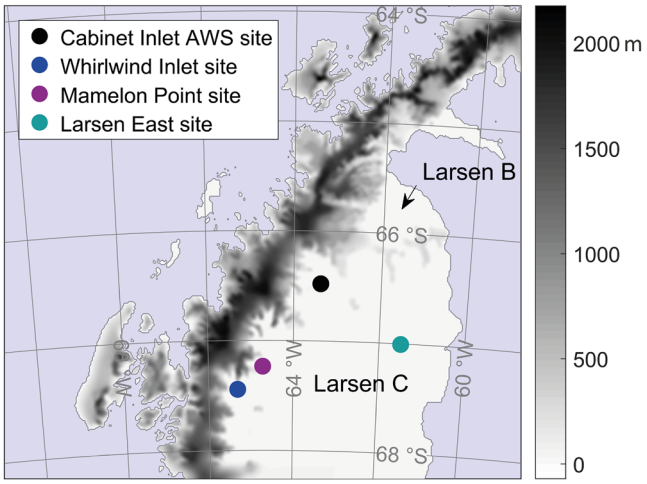

Figure 1. Map of the model domain showing the orography of the Antarctic Peninsula (gray scale is terrain height), the majority of Larsen C and the remaining section of Larsen B (in white), and the locations of focal sites (see legend). Note that all observations used in this study come from the Cabinet Inlet AWS site, while all four sites are used for model data analysis. The sea is shown in light blue. The land-sea mask and orography data used here are the same as that used for the model simulation; see section 2.2.

nighttime foehn, SH has dominated across much of the ice shelf (Elvidge, 2013; Kuipers Munneke et al., 2018). During daytime summer foehn, the two terms have either roughly canceled in inlets (Grosvenor et al., 2014) and toward the eastern edge of Larsen C (King et al., 2017; Kuipers Munneke et al., 2012), or LH has dominated (Elvidge, 2013). Relating this balance of SH and LH to meteorological conditions needs clarification.

- The fact that the highest melt rates are observed within the inlets has been hypothesized to be due to the incidence of the strongest foehn winds—foehn jets—in these inlets. However, the validity of this hypothesis depends on the net turbulent surface heat flux during foehn, which, as established above, is as yet unclear. Furthermore, this hypothesis conflicts with the observed spatial variability in foehn air temperatures, which are typically lower in the jets than in wake regions due to a dampened foehn effect in the jets (Elvidge et al., 2015; Elvidge & Renfrew, 2016). In fact, of the two studies addressing the SEB impact of foehn jets, Elvidge (2013) found less melt in the inlets, while Grosvenor et al. (2014) found no clear influence of jets on melt rates. However, these papers only consider a small number of case studies, which are not necessarily representative.

The goal of this study is to quantify and explain the atmospheric drivers of melt across Larsen C and consequently to reconcile the above contradictions, using new, ideally located observations together with a long-duration, high-resolution, state-of-the-art model simulation. Section 2 provides summaries of the data and details a novel method we have devised to investigate the problem. In section 3 we characterize the meteorological conditions, SEB, and melt at a representative inlet across three melt seasons. In section 4 we identify distinct SEB regimes and explore their characteristics and influence during both foehn and non-foehn conditions. In section 5 we investigate the local meteorological controls on melt during foehn. Following a brief evaluation of model performance in sections 3 and 5, in section 6 we focus on the model data to explore the drivers of melt across the ice shelf as a whole. Section 7 summarizes and concludes the study.

2. Data and Methods

The observations in this study are from an automatic weather station (AWS) located in Cabinet Inlet (Figure 1). These observations cover three austral summer seasons over 31 continuous months from the AWS's installation date of 25 November 2014 to 17 June 2017, at half-hourly resolution. The model output is from a limited area simulation of the Met Office Unified model (MetUM), covering the domain shown in Figure 1 from 25 November 2015 to 31 May 2016. These dates were chosen to encompass the majority of one summer melt season; 96% of annual (July 2015 to June 2016) melt in the AWS observations

occurred during this period. In both observational and model data, foehn conditions have been diagnosed according to a location-dependent criterion based on wind direction and relative humidity (see Appendix A for details and justification).

2.1. AWS Data

The AWS is jointly operated by the Institute for Marine and Atmospheric Research of Utrecht University (UU/IMAU) and the British Antarctic Survey (BAS) and is known as IMAU AWS 18. It is located at 66°24′S, 63°22′W at a height of ~70 m above mean sea level. It has sensors for air and surface temperature, air pressure and humidity; an acoustic snow height sensor; a propeller-vane anemometer measuring wind direction and speed; and a radiometer for measuring downward and upward shortwave and longwave radiative fluxes. A bulk-algorithm-based SEB model (Kuipers Munneke et al., 2009) has been used to derive surface SH and LH fluxes and the ground heat flux. The energy available for melt is also derived from this model, given as the SEB residual when the surface temperature, T_{sfc}, is above freezing point:

$$\mathrm{melt}_{SEB} = \begin{cases} 0, & T_{sfc} < 0°C \\ \max(0,\ SW + LW + SH + LH + GH), & T_{sfc} = 0°C, \end{cases}$$

where SW, LW, SH, LH, and GH are the net surface fluxes of, respectively, shortwave radiative heat, longwave radiative heat, sensible heat, latent heat, and ground heat, here given as positive when directed toward the surface, and T_{sfc} is the surface temperature. Reported quantities are at nominal levels of 2 m for temperature and humidity and 10 m for wind speed, adjusted from the raw measurements typically made between 1.7 and 2.4 m.

Several quality checks and corrections have been applied to the AWS data. Solar radiation observations were tilt corrected (Wang et al., 2016) and further constrained by calculating a 24-hr running mean albedo following Van den Broeke et al. (2004). By inspecting data from the upward-facing longwave radiation sensor, we found that no rime accreted on the radiation sensors at this location. Air temperature observations, performed inside naturally ventilated radiation shields, were corrected downward during periods of sunny weather with little or no wind, following the method of Smeets et al. (2018). Compared to direct eddy correlation observations of turbulent fluxes (e.g., by using a 3-D ultrasonic anemometer), the bulk method that we apply to the AWS observations yields similar results; with a root-mean-square difference of typically 3–4 W m^{-2} at Antarctic sites experiencing frequent air flow (e.g., Van den Broeke et al., 2005). With the wind sensor being at a height of 2–3 m, the bulk method captures most of the turbulent eddies, and does not severely violate the assumption of constant flux in the layer between the surface and the instrument height.

2.2. Model Data

The MetUM is a state-of-the-art, nonhydrostatic atmospheric model used by the Met Office for operational weather forecasting and as a component in all their climate models (Walters et al., 2019). Here, we have used Version 10.6 of the MetUM and a standard parameterization configuration (generally following Tang et al., 2013). This configuration has proven reasonably accurate at simulating cases of orographic flows over Antarctica (e.g., Elvidge & Renfrew, 2016; Elvidge et al., 2016, 2015; Orr et al., 2014). Instead of the model defaults, the land-sea mask was derived from the SCAR Antarctic Digital Database coastline, Version 7.0 (released January 2016 and available at https://www.add.scar.org/), and the orography was derived from the high-resolution Radarsat Antarctic Mapping Project (RAMP; Liu et al., 2015) digital elevation model.

The limited area model simulation has a horizontal grid spacing of 1.5 km and 70 vertical levels (the lowest of which is at a height of 2.5 m over the ocean and there are 16 levels in the lowest km). This resolution is the same as or higher than those used for previous model studies of individual foehn events over Larsen C (e.g., Elvidge et al., 2016, 2015; Grosvenor et al., 2014; Turton et al., 2017) and is significantly higher than those used for previous model climatologies spanning one or more melt seasons (e.g., Datta et al., 2019; King et al., 2017). Note that this model does not incorporate a multilayer snow scheme. Consequently, a best estimate of melt in the model is provided by melt_{skin}, the residual energy available for surface melt, following King et al. (2008) and Kuipers Munneke et al. (2012) in assuming that ground heat flux contributions are negligible:

$$\mathrm{melt}_{\mathrm{skin}} = \begin{cases} 0, & T_{\mathrm{sfc}} < 0°\mathrm{C} \\ \max(0, \mathrm{SW} + \mathrm{LW} + \mathrm{SH} + \mathrm{LH}), & T_{\mathrm{sfc}} = 0°\mathrm{C} \end{cases}.$$

In our analysis of the model data, four sites of focus are chosen (see Figure 1 for locations):

- The Cabinet Inlet IMAU AWS18 site, 66°24′S, 63°22′W
- Whirlwind Inlet, 67°27′ S, 65°18′ W—situated in another foehn-prone Larsen C inlet.
- Mamelon Point, 67°14′S, 64°42′W—situated between Whirlwind Inlet to the south and Mill Inlet to the north in a region known to typically experience wake conditions during foehn (Elvidge et al., 2015).
- Larsen East, 67°01′S, 61°29′W—situated toward the eastern edge of Larsen C, approximately 150 km east of the AP, and the site of IMAU AWS14, data from which have been used in several previous studies (e.g., Elvidge, 2013; King et al., 2015; Kuipers Munneke et al., 2012; Turton et al., 2018; Van den Broeke, 2005).

2.3. SEB Regimes

Determining the atmospheric drivers of melt over climatological timescales is complicated by nonlinear interactions and feedbacks between SEB components and meteorological conditions. To overcome this challenge, we have categorized the SEB into distinct regimes determined by which SEB component is *dominating* and in which direction. An SEB component is said *to dominate* when it is contributing a heat flux which is greater in magnitude than all of

a Each of the individual contributions of the other components
b The combined contribution of all other components
c 50 W m^{-2}

For example, the following logical expression determines whether or not the downward SH-dominated regime ($\mathrm{SEB}_{\downarrow\mathrm{SH}}$) is occurring:

$$\mathrm{SEB}_{\downarrow\mathrm{SH}} = \begin{cases} \text{occurring}, & \{\mathrm{SH} > 50\ \mathrm{W\,m^2}\}\ \textit{and}\ \{\mathrm{SH} > |\mathrm{LH}|\}\ \textit{and}\ \{\mathrm{SH} > |\mathrm{SW}|\}\ \textit{and}\ \{\mathrm{SH} > |\mathrm{LW}|\}\ \textit{and}\ \{\mathrm{SH} > |\mathrm{LH} + \mathrm{SW} + \mathrm{LW}|\} \\ \text{not occurring}, & \text{otherwise.} \end{cases}$$

Equivalent expressions are used for all other possible regimes, of which there are eight in total (that is, SEB domination by each of the four components, in each direction). Of these regimes, only four occur in our data: $\mathrm{SEB}_{\downarrow\mathrm{SH}}$, $\mathrm{SEB}_{\uparrow\mathrm{LH}}$, $\mathrm{SEB}_{\downarrow\mathrm{SW}}$, $\mathrm{SEB}_{\uparrow\mathrm{LW}}$, where ↓ and ↑ denote downward and upward flux directions, respectively. Note that the SEB is often not dominated by any single component, but during such conditions the net flux is typically small (92% of the time smaller than ±25 W m^{-2}) and consequently relatively little melt occurs (only 6% of total melt in the Cabinet Inlet observations and only 2% of total melt at the four sites of focus in the model). Note that our results are not qualitatively sensitive to the value of the fixed heat flux threshold, though we find the chosen value of 50 W m^{-2} to be optimal in yielding useful results for the attribution of melt to atmospheric drivers as it strikes a balance between being sufficiently large to ensure significant differences in SEB composition between regimes and sufficiently small to ensure that little melt occurs when no SEB component is dominating.

3. Meteorological Conditions and Surface Energy Exchange in Cabinet Inlet

Here we investigate the seasonal variability in atmospheric conditions and the broad meteorological drivers of melt at Cabinet Inlet.

Figure 2 shows that the two most frequent wind directions in the Cabinet Inlet observations are northwesterly and southerly. During melt, winds are most commonly westerly to northwesterly. Both the highest wind speeds and the highest melt rates occur in westerly to northwesterly flow, consistent with foehn (and sometimes katabatic winds; see Appendix A) drawn down the eastern slopes of the AP. A second peak in wind speeds is found in southerly wind directions, consistent with cold, southerly barrier flows along the east coast of the AP (see Parish, 1983; Schwerdtfeger, 1975). Modeled wind and melt distributions are qualitatively similar to the observations, although the model underestimates winds and melt in the westerly sector.

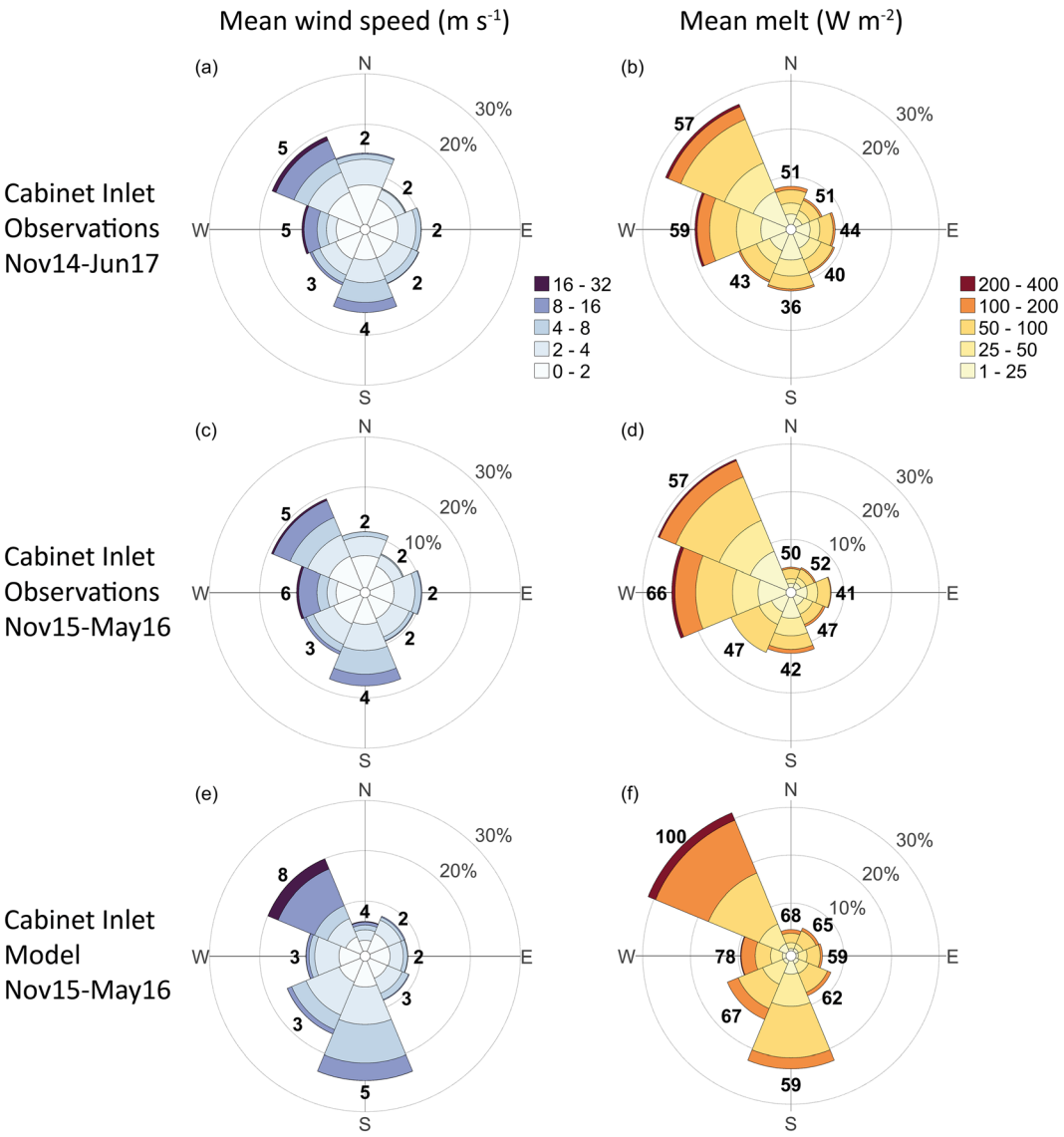

Figure 2. Rose charts summarizing the distributions of wind speed, wind direction, and melt at Cabinet Inlet. (a, c, and e) Wind roses, with colors denoting the distribution of wind speeds (m s^{-1}) and bold numbers giving the mean wind speed for each segment. (b, d, and f) "Melt roses" showing melt for each wind direction segment as a percentage of total melt, the distribution of melt rates (color), and mean melt rates (numbers in bold; W m^{-2}). The data used are (a, b) all available AWS observations, (c, d) the AWS observations between 25 November 2015 and 31 May 2016 (the period of the model simulation), and (e, f) the model simulation. Note that $melt_{SEB}$ is used for panel (b) and $melt_{skin}$ is used for panels (d) and (f), and only values of $melt_{SEB}$ and $melt_{skin}$ greater than 1 W m^{-2} are included.

Statistics and monthly variability in foehn and melt occurrence and melt rates from all AWS observations are presented in Figures 3a and 3b and Table 1. At Cabinet Inlet, foehn occurs 15% of the time and is responsible for 45% of the melt (Table 1). The potency of foehn in causing melt reflects both elevated melt occurrence (3 times more common) and elevated rates of melt when melt is occurring (1.4 times greater) during foehn than non-foehn conditions (note these differences are statistically significant at the 99% level). While foehn occurs all year round at Cabinet Inlet (Figure 3), our observations corroborate previous studies (e.g., Datta et al., 2019; King et al., 2017; Turton et al., 2018; Wiesenekker et al., 2018) in showing it to be least common during the summer (4% of the time in December) and most common in midspring (peaking at 32% in October) and autumn (20% in May). Foehn explains 88% of total melt occurring outside of the summer months (December–February, DJF), of which 98% occurs during the spring (September–November, SON) and autumn (March–May, MAM). It is worth noting that the strong influence of foehn

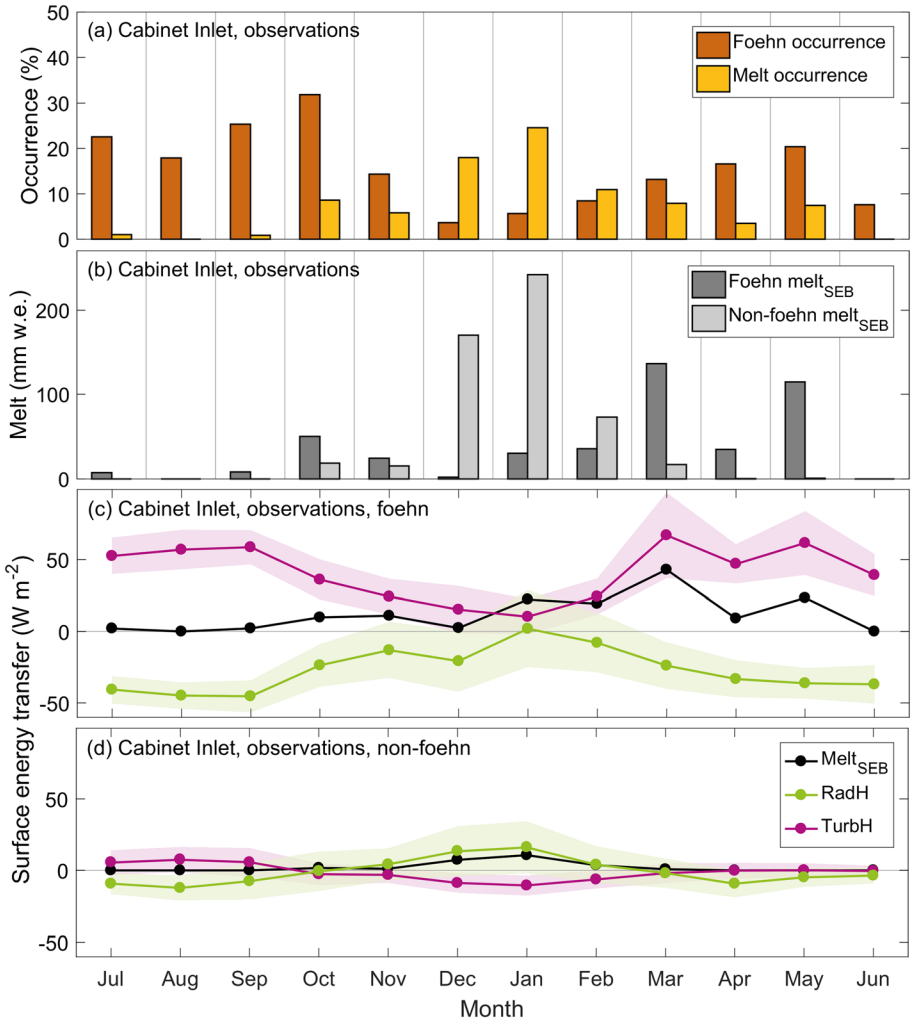

Figure 3. Monthly mean time series of all available AWS observations at the Cabinet Inlet site (November 2014 to June 2017), showing (a) monthly foehn and melt$_{SEB}$ occurrence (as a percentage of time), (b) monthly accumulation of melt during both foehn and non-foehn conditions, and (c, d) monthly mean melt$_{SEB}$ and net downward radiative and turbulent surface heat fluxes during (c) foehn and (d) non-foehn conditions, with standard deviations in these fluxes indicated by shading.

during the spring is also likely to play an important role in preconditioning the ice shelf for summertime melt via reduced albedo due to the warming, coarsening and melting of the top layers of snow (e.g., Kuipers Munneke et al., 2014). During foehn, the SEB typically comprises a balance between heat gain via the net turbulent heat flux (TurbH), and heat loss via the net radiative heat flux (RadH) (Figure 3c); with the mean turbulent term greater in magnitude than the mean radiative term during all months except December. The foehn SEB is most strongly dominated by TurbH during March, coinciding with the highest mean melt rates during foehn. Interestingly, there is no evidence for the foehn cloud-clearance effect in the Cabinet Inlet observations; the average proportion of solar irradiance at the top of the atmosphere reaching the surface (SW_{Sfc}/SW_{TOA})—a proxy for cloud cover—is similar under foehn conditions to that under non-foehn conditions (see Table 1).

Roughly half of annual melt at Cabinet Inlet occurs during the summer months (DJF), 88% of which is during non-foehn conditions. The non-foehn monthly mean SEB comprises a balance between downward RadH and upward TurbH (Figure 3d).

For the single melt season covered by the simulation, the observed monthly variability in foehn occurrence, melt, and SEB components (Figure 4a) are generally consistent with those described above for the

Table 1
Foehn, melt and solar radiation statistics at the focal sites on Larsen C

	25 Nov. 2014 to 17 June 2017	25 November 2015 to 1 June 2016				
	Obs, CI	Obs, CI	Model, CI	Model, WI	Model, MP	Model, LE
Foehn occurrence (% of time)	15	18	17	26	9	9
Melt occurrence (% of time)	8	13	14	15	10	14
Melt occurrence during foehn (% of time)	20	35	29	23	16	20
Melt occurrence during non-foehn (% of time)	6	8	11	12	10	13
Mean melt rate during foehn melt (W m^{-2})	61	62	102	99	77	73
Mean melt rate during non-foehn melt (W m^{-2})	43	45	62	54	59	63
Accumulation of foehn-driven melt (mm w.e.)	446	195	245	290	54	63
Accumulation of non-foehn-driven melt (mm w.e.)	539	150	287	231	257	368
Median SW_{Sfc}/SW_{TOA} during foehn	0.50	0.54	0.64	0.67	0.74	0.67
Median SW_{Sfc}/SW_{TOA} during non-foehn	0.52	0.52	0.58	0.56	0.58	0.63

Note. Data are derived from observations ("Obs") and the model for the Cabinet Inlet (CI) site, and from the model for the Whirlwind Inlet (WI), Mamelon Point (MP), and Larsen East (LE) sites. All statistics are given for the entire period covered by the simulation (25 November 2015 to 1 June 2016), and those for the observations are additionally given for the entire observation period (25 November 2014 to 17 June 2017). "Melt" is given as $melt_{SEB}$ in the column for 25 November 2014 to 17 June 2017, and as meltskin in the column for 25 November 2015 to 1 June 2016. Top of atmosphere solar irradiance (SW_{TOA}) is model-derived. The differences in SW_{Sfc}/SW_{TOA} between foehn and non-foehn conditions are significant at the 99 % level according to the Mann-Whitney U test (in all cases but the Cabinet Inlet observations, where the difference is small, and the Larsen East model data, which are limited by the foehn sample size).

three-season mean. During this single season, the differences between $melt_{SEB}$ and $melt_{skin}$ in the observations (Figure 4a) are generally negligible relative to the differences in observed $melt_{skin}$ and simulated $melt_{skin}$ (Figures 4a and 4d). This suggests that the omission of ground heat flux in the model is a relatively minor source of model error. Recall the penetration and absorption of SW below the surface of the snowpack is accounted for in $melt_{SEB}$ but not in $melt_{skin}$ (Kuipers Munneke et al., 2012).

The model generally performs well. Figures 4a and 4d show that the monthly occurrence of foehn is accurately reproduced; the bias never greater than ±7% and the difference during the entire melt season being only 1% (Table 1). Monthly melt occurrences during all (foehn and non-foehn) conditions are also generally handled well (though with notable biases in December and May), with a melt-season difference also of only 1%. Monthly mean variability in the SEB contributions from TurbH and RadH are qualitatively well represented; The seasonal timings of peaks and troughs are generally accurate, as are the key differences in these fluxes between foehn and non-foehn conditions (Figures 4b, 4c, 4e, and 4f). Despite a consistent positive bias during foehn, TurbH is also generally quantitatively accurate. During foehn conditions, the monthly bias in TurbH is less than 20 W m^{-2} for all months except January, while during non-foehn conditions the monthly bias is always <5 W m^{-2}.

In RadH, however, the model exhibits significant biases. During DJF there is typically a positive model bias in mean downward SW and consequently RadH, leading to exaggerated monthly melt rates during both foehn and non-foehn conditions (Figures 4b, 4c, 4e, and 4f). This overestimation is most significant for non-foehn conditions, with the total accumulation of melt during the 2015–2016 melt season being 150% of that observed. The overestimation is smaller in the accumulation of foehn-driven melt (the simulated value being 126% of the observed value), reflecting less dependence on RadH during foehn. Note that significant model biases in RadH over Larsen C have been found in previous studies (e.g., Gilbert et al., 2020; Grosvenor et al., 2014; King et al., 2015; Kirchgaessner et al., 2019). Unlike in the observations, there is evidence for the cloud-clearance effect in the model, with SW_{Sfc}/SW_{TOA} being significantly greater during foehn than during non-foehn conditions (Table 1). This will account for a portion of the model bias in RadH during foehn conditions (N.b. the size of this portion cannot easily be ascertained, and further discussion on the sources of model error is beyond the scope of this study).

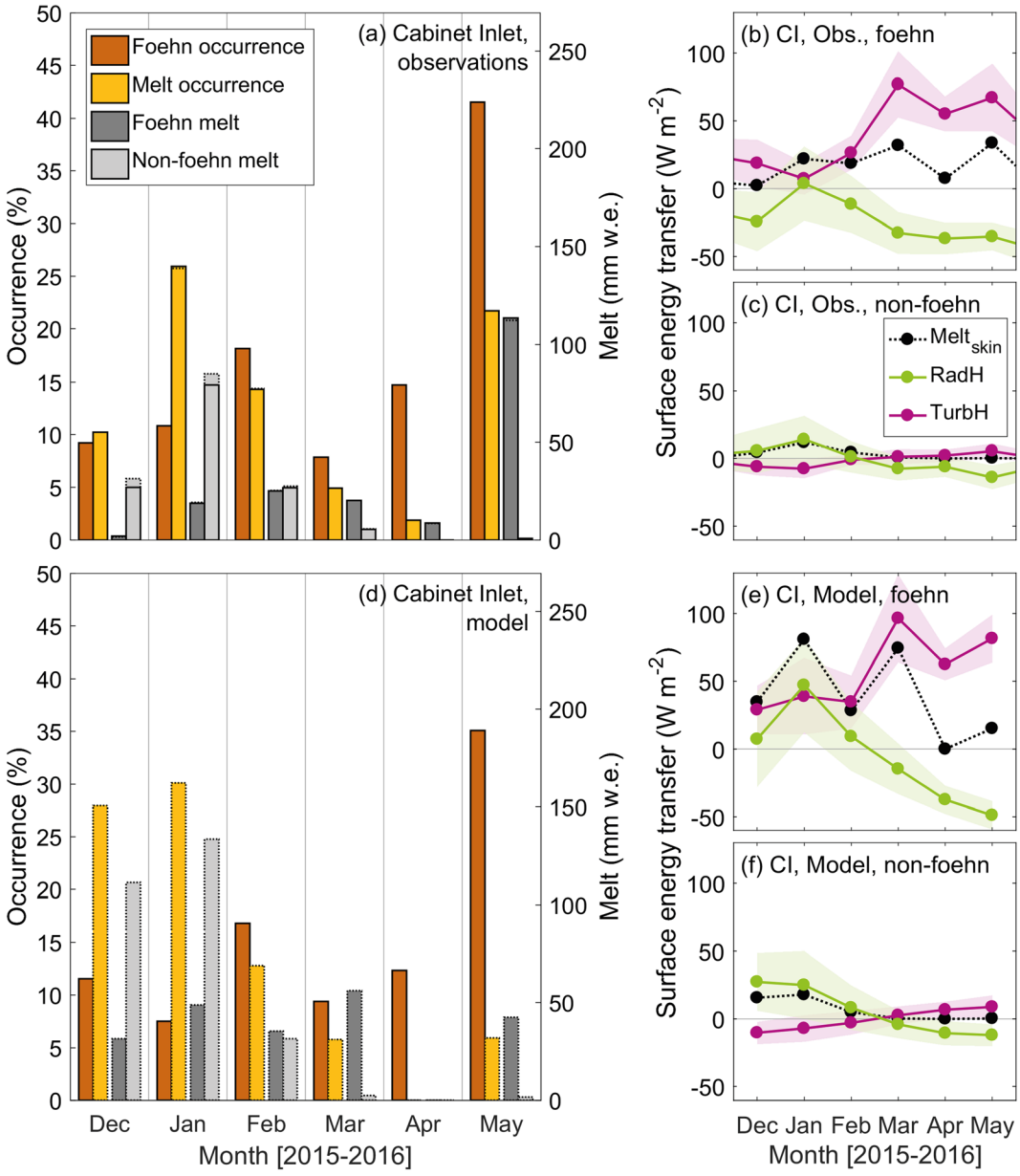

Figure 4. Monthly mean time series between December 2015 and May 2016 for the Cabinet Inlet site (CI) of (a–c) observed and (d–f) modeled (a, d) monthly foehn and $melt_{SEB}$ occurrence (as a percentage of time; left axis) and monthly accumulation of melt during both foehn and non-foehn conditions (right axis) and (b–c, e–f) monthly mean melt and net downward radiative and turbulent surface heat fluxes during foehn and non-foehn conditions, with standard deviations in these fluxes indicated by shading. Melt is given as $melt_{SEB}$ for solid bar borders in (a, d), and as $melt_{skin}$ for dotted bar borders in (a) and (d) and dotted black lines in (b) and (c), and (e) and (f).

4. SEB Regimes in Cabinet Inlet

We categorize the ice shelf SEB observed in Cabinet Inlet into regimes according to which component is *dominating*, as described in section 2.3. We explore the sensitivity of SEB regime occurrence to meteorological conditions and the sensitivity of surface temperature and melt to the SEB regime. Figure 5 shows the prevalence of each SEB regime and their contributions to mean and cumulative (i.e., time-integrated) surface energy exchange and melt, for all available Cabinet Inlet observations.

During foehn conditions (Figures 5a and 5b), the SEB is typically positive (surface heating) and is commonly (62% of the time) dominated by a single component, with typically greater flux contributions by individual

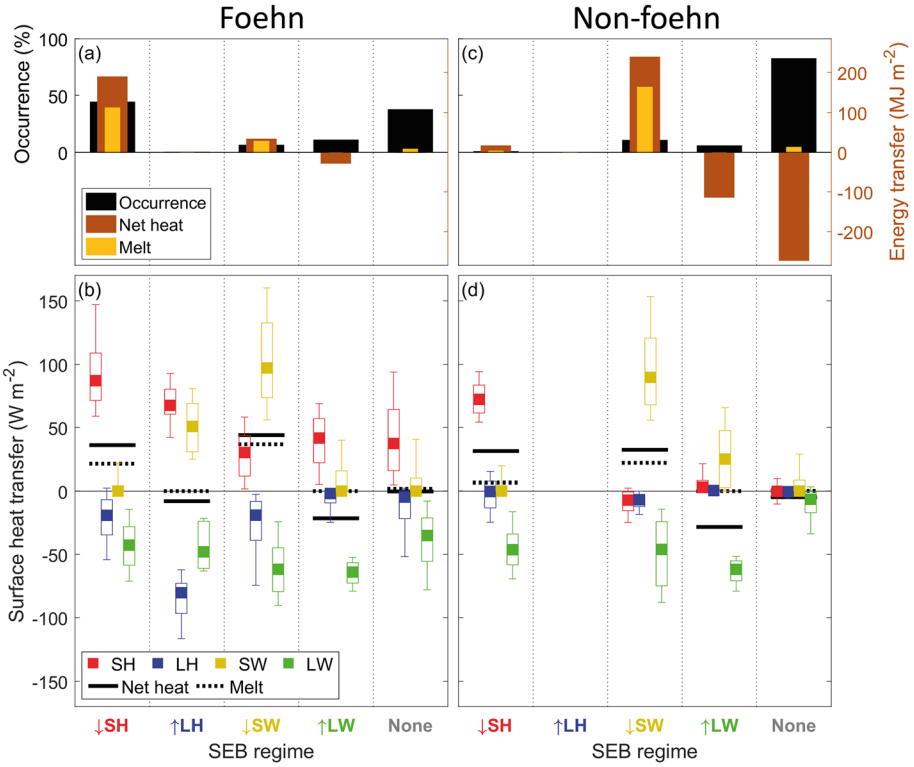

Figure 5. Prevalence and contributions to the SEB and melt for each SEB regime during foehn and non-foehn conditions, from all available Cabinet Inlet AWS observations (November 2014 to June 2017). In (a) and (c), black bars give the percentage of time during which each regime occurs (left axis), while brown and orange bars give cumulative (i.e., time-integrated) contributions to net downward heat transfer and $melt_{SEB}$, respectively (right axis). In (b) and (d), black, solid horizontal lines denote the mean net heat flux, black dotted lines denote the mean energy available for melt, and box and whiskers show the median, interquartile range and 9th and 91st percentiles of each SEB component. The SEB regime "none" denotes where no single SEB component dominates (see section 2.3). Note that $SEB_{\uparrow LH}$ never occurs during non-foehn conditions.

SEB components than during non-foehn conditions. The $SEB_{\downarrow SH}$ regime is most common and is responsible for most cumulative surface warming and melt (76%). Nonetheless, significant contributions to melt during foehn are driven by solar radiation in the $SEB_{\downarrow SW}$ regime (19% of the cumulative total), despite this regime only occurring 6% of the time during foehn. The strong surface heating and melting seen in this regime is largely due to the SW fluxes being commonly supported by smaller but significant downward SH fluxes. During both the $SEB_{\downarrow SH}$ and $SEB_{\downarrow SW}$ regimes, smaller upward fluxes in LW and LH tend to partially offset the downward fluxes. The second most common SEB regime during foehn is $SEB_{\uparrow LW}$, in which upward LW fluxes—partially offset by downward SW fluxes—lead to net surface cooling. Very rarely (<1% of the time) the $SEB_{\uparrow LH}$ regime occurs. This is when sublimation is the dominant energy exchange process and is characterized by significant flux contributions from all the SEB components, leading on average to weak surface cooling.

During non-foehn conditions (Figures 5c and 5d), for the majority (83%) of time, no single component dominates the SEB, the net SEB is typically close to 0 and, overall, imparts a weak net cooling effect, which amounts to a significant cumulative surface cooling over the course of the full observational record. For the remainder of the time, the radiative flux components tend to dominate; with the $SEB_{\downarrow SW}$ and $SEB_{\uparrow LW}$ regimes occurring 11% and 6% of the time, respectively. During $SEB_{\downarrow SW}$, downward SW fluxes—typically partially offset by weaker upward LW fluxes—contribute a significant net surface warming effect and the vast majority (>90%) of melt occurring during non-foehn conditions. Conversely, during $SEB_{\uparrow LW}$, upward LW fluxes—typically partially offset by weaker downward SW fluxes—contribute a net surface cooling effect and no melt.

It is notable that during non-foehn conditions nearly all melt occurs in a radiative dominated regime ($SEB_{\downarrow SW}$), while during foehn conditions significant melt occurs during both radiative ($SEB_{\downarrow SW}$) and turbulent ($SEB_{\downarrow SH}$) dominated regimes. As a consequence, the relationship between meteorological conditions and melt is more complex during foehn conditions. As outlined in section 1, this complexity is evident in the diversity of results from previous studies on foehn melt signatures, especially those of foehn-jet-prone inlets as distinct from those of neighboring wake regions. In the next section we investigate this further, aiming to clarify uncertainty in the sensitivity of foehn-driven surface warming and melt to meteorological conditions.

5. Meteorological Controls on Melt During Foehn in Larsen C Inlets

It has been shown in sections 3 and 4 that the foehn SEB at Cabinet Inlet is typically dominated by SH, which in turn is governed by wind speed and the air-surface temperature gradient. On this basis, we now test the following hypothesis:

During foehn over Larsen C, variability in the SEB and melt depends principally on foehn wind speed and the temperature of the incoming foehn air relative to that of the ice surface.

Figure 6 shows the sensitivity of the SEB components and melt to wind speed for both the observational and model data. The analysis is split into two subsets using static stability (expressed as the square of the Brunt-Väisälä frequency, N) between the surface and 2 m for the observations and between the surface and 1.5 m for the model. These subsets represent (i) typical *stably stratified foehn* conditions and (ii) rare *weakly stratified foehn* conditions. The static stability threshold used to divide the data into these subsets is chosen to be the approximate value of N^2 at which the largest contributor to surface heating transitions between SW and SH (this value is determined by averaging the fluxes across N^2 bins of interval 0.01 s^{-1}). This is, for the observations and model respectively, 0.05 (the 5th percentile in N^2; that is, only 5% of foehn occurring is *weakly stratified*) and 0.07 s^{-1} (the 16th percentile in N^2).

In the *stably stratified foehn* subset of the Cabinet Inlet observations, TurbH generally dominates over RadH; SH-driven surface heating characterizes conditions in all but the weakest winds (<3 m s^{-1}), in which LW-driven surface cooling generally prevails (Figure 6a; though note that for simplicity the radiative heat fluxes are combined in Figure 6). As winds strengthen, SH increasingly dominates the SEB, leading to increasing surface heating and melting. Conversely, in the *weakly stratified foehn* subset, generally downward SH is canceled by upward LH, and RadH dominates over TurbH, with SW-driven surface heating typifying the SEB when wind speeds are <12 m s^{-1} (Figure 6b). As winds strengthen, the influence of LH increases, leading to a decrease in net heating and melting, and culminating in an approximate balance in SEB components above 12 m s^{-1}. The SEB sensitivities to wind speed and static stability observed at Cabinet Inlet are generally well represented by the model (Figures 6c and 6d). Furthermore, these sensitivities are very similar at Whirlwind Inlet (Figures 6e and 6f)—which implies they are likely to apply to all Larsen C inlets during foehn. Note that *weakly stratified foehn* at Cabinet Inlet is three times more likely in the model than the observations. This reflects the positive model bias in SW leading to weaker summertime static stabilities (see section 3).

Physical explanations for the relationships between SEB and foehn conditions are now discussed with the aid of the schematics shown in Figure 7. In typical foehn conditions over Larsen C, warm air passes over cold ice (the maximum temperature of which is limited by the melting point). In moderate to strong winds this results in SH-driven net surface warming and melt (Figure 7a). In weak winds the surface becomes largely decoupled from the warm foehn and LW-driven net cooling prevails (Figure 7b). In cases where the foehn air is cooler than usual and/or is flowing over radiatively warmed ice, the temperature gradient will be too small for SH to dominate, no matter what the wind speed. Instead, the role of SH becomes reactive, varying such as to minimize changes in surface temperature relative to air temperature. And it becomes more effective in this role as the wind speed and wind-induced turbulence increases, until the net SEB is reduced to near-zero (Figures 6b, 6d, and 6f), often with large flux contributions from all SEB components (Figure 7c). During foehn characterized by weak winds and weak-stratification, SW-driven net surface warming and melt prevails and helps to maintain the low static stabilities (Figure 7d).

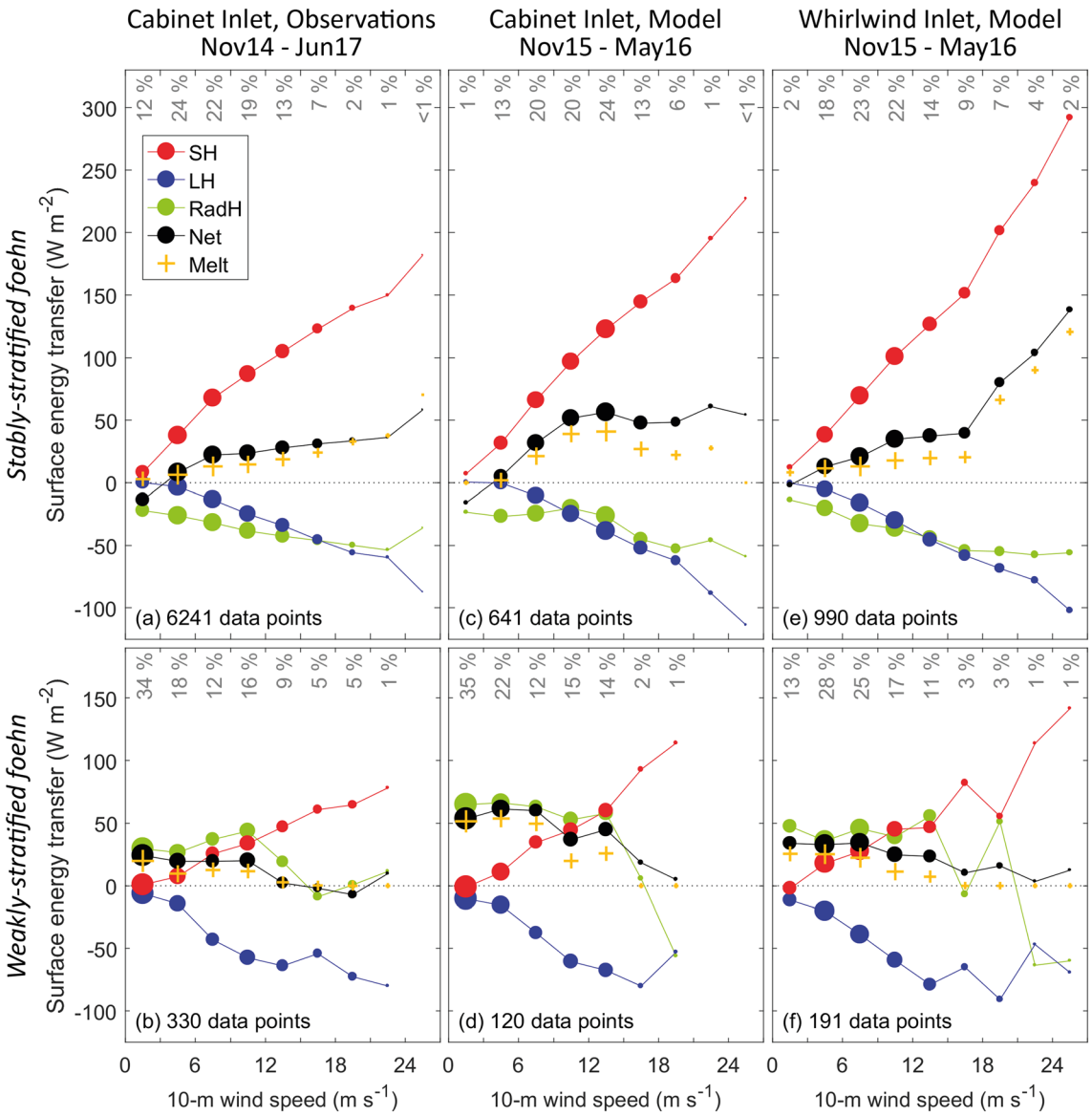

Figure 6. Surface energy components as a function of wind speed for *stably stratified foehn* conditions (top) and *weakly stratified foehn* conditions (bottom) during (a, c, and e) *stably stratified foehn* and (b, d, and f) *weakly stratified foehn*, from (a, b) all Cabinet Inlet observations, (c, d) all Cabinet Inlet model data, and (e, f) all Whirlwind Inlet model data. Data are binned according to wind speed. The number of data points in each wind speed bin is denoted by the size of the plot markers and also given toward the top of each panel as a percentage of the total number of data points in each panel, which is itself stated at the bottom of each panel. Melt is given as $Melt_{SEB}$ in (a) and (b) and as $Melt_{skin}$ in (c)–(f).

The hypothesis proposed at the start of this section has been proven. The nonlinear relationship between net SEB and foehn conditions can be explained by differences in wind speed, the influence of which is modulated by the warmth of incoming foehn relative to the ice surface, via TurbH. These wind speed sensitivities largely explain the SEB differences between foehn-jet-prone inlets and adjacent wake regions. Other notable meteorological factors contributing to these SEB differences include the likelihood of more frequent and persistent foehn in inlets than in wake regions due to the funneling effect of local orography, and jet-wake differences in temperature and humidity (jet air typically being cooler and moister; Elvidge et al., 2015). The likely climatological effect of the former is enhanced foehn-driven melt in inlets relative to wake regions, while that of the latter is reduced foehn-driven melt in inlets relative to wake regions.

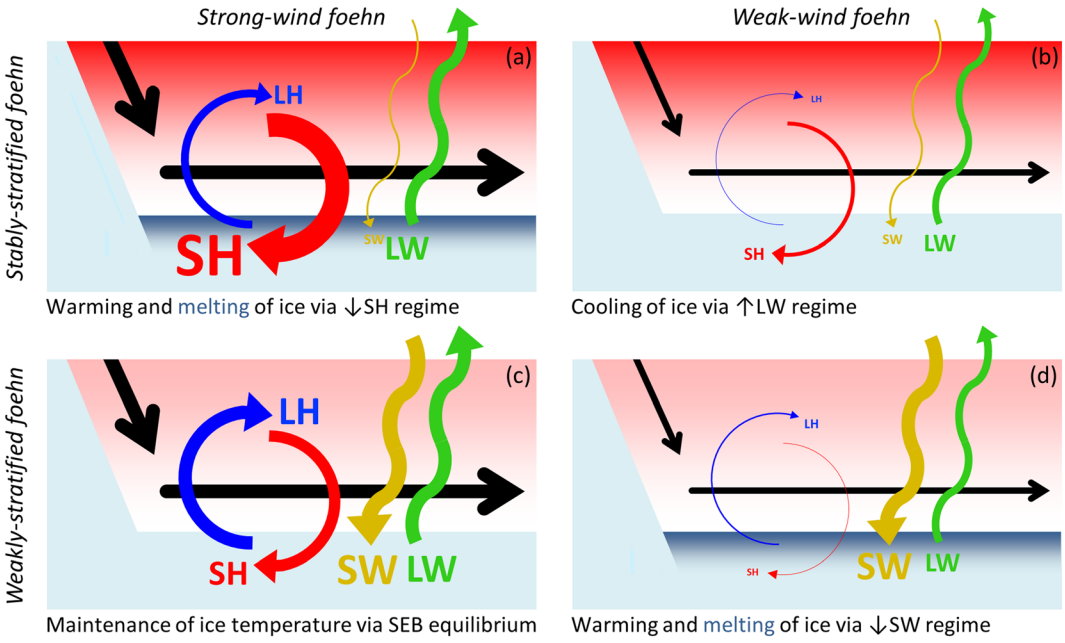

Figure 7. Schematics representing foehn SEB sensitivity to wind speed during (a, b) typical, *stably stratified foehn* conditions and (c, d) *weakly stratified foehn* conditions. The black arrows denote the foehn winds in the lower atmosphere (white to red shades; darker reds denoting warmer air) descending the eastern slopes of the AP and then advancing across the ice shelf (light blue), with thicker arrows denoting stronger winds. The colored arrows denote heat fluxes, with their widths and label font sizes proportional to the absolute, mean observed values at Cabinet Inlet. These values range in magnitude from 0.5 W m^{-2} (for LH in *weak-wind stably stratified foehn* conditions) and 113 W m^{-2} (for SH in *strong-wind stably stratified foehn* conditions). The SEB net effect(s) of each foehn classification on the ice shelf are described below each panel, and the occurrence of significant melt is also denoted by dark blue shading at the top of the ice shelf in panels (a) and (d). Mean melt rates are, for (a), (b), (c) and (d) respectively, 22, 4, 2 and 16 W m^{-2}. Foehn classifications are defined using the same Brunt-Väisälä frequency threshold as used for Figure 6 (the 5th percentile) to distinguish between *stably stratified foehn* and *weakly stratified foehn*, and the 25th and 75th wind speed percentiles (4.5 and 11.6 m s^{-1}, respectively) to distinguish between *strong-wind foehn* and *weak-wind foehn*.

If we consider the high-resolution model simulation of summertime foehn ("Case A") presented in Elvidge (2013) and also studied in Elvidge et al. (2016, 2015), surface temperatures in the inlets were, relative to the rest of the foehn-effected ice shelf, high during the night and low during the day. Melt only occurred during the daytime, and melt minima were found in the inlets. This particular event was characterized by relatively low near-surface foehn air temperatures (typically 1–2°C in inlets; corresponding to the 2nd to 5th percentiles of foehn air temperatures during melt in our observations). Consequently, during the daytime *weakly stratified foehn* prevailed (cf. Figure 7d), characterized by SW-driven surface warming and melt that was lower beneath the jets than elsewhere. During the nighttime, *stably stratified foehn* prevailed, with more surface warming beneath the jets than elsewhere, but with foehn air temperatures insufficiently high to cause melting. In addition to the diurnal effect on surface static stabilities, foehn jet air temperatures were lower (by 3–4 K) than the air temperatures in adjacent wakes. Consequently, all else being equal, the jet SEB was more likely than the wake SEB to fall into the *weakly stratified foehn* state. In contrast, the foehn case studied by Kuipers Munneke et al. (2018) was characterized by near-surface air temperatures in excess of 10°C (the 95th percentile in our observations) and significant melt in the Larsen C inlets. Clearly this was a case of *stably stratified foehn* (cf. Figure 7a) and would have remained so even in the presence of strong solar forcing.

The high sensitivity of the net SEB during foehn to wind speed and static stability may also help to explain why the model climatology of King et al. (2017) was unable to reproduce observed Larsen C melt distributions. Little evidence of foehn jets was found in their model wind speed data, and the model they used (the Antarctic Mesoscale Prediction System) is known to struggle in representing the relationship between wind speed and static stability over an ice shelf (Wille et al., 2016). Further discussion on the challenges of model representation of the Larsen C SEB is presented in section 7.

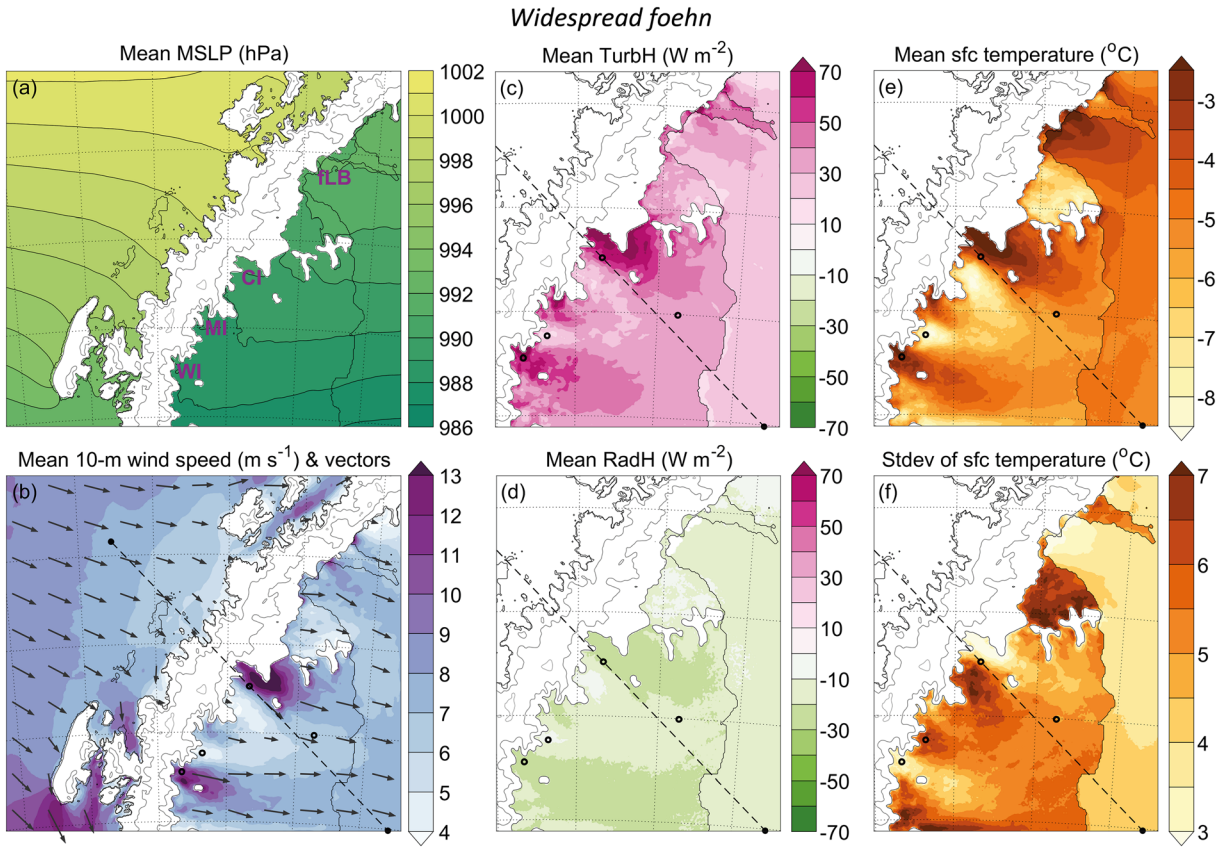

Figure 8. Model composite spatial plots during *widespread foehn* conditions (which occur 12% of the time) across the Antarctic Peninsula for the 2015/2016 melt season. In each panel, the field plotted is given by the title; note here that "MSLP" stands for "mean sea level pressure," "sfc" stands for "surface" and "stdev" stands for "standard deviation." Orography contours are also plotted in gray scale (c.f. Figure 1). In (a), four inlets are labeled (CI: Cabinet Inlet; WI: Whirlwind Inlet; MI: Mill Inlet; fLB: former Larsen B embayment), while the locations of the four data sites are shown in the other panels (open black circles; see Figure 1 for site names). The dashed line linking solid black circles marks the transect used for the Figure 9 cross sections. Note that in panels (c)–(f) a smaller domain at larger scale is presented, and data are only shown to the east of the AP. In all panels, data are masked out where terrain height exceeds 100 m in all panels and also west of the AP in panels (c)–(f).

6. Drivers of Melt Across Larsen C

In this section, our investigation of the drivers of melt is extended to the entire ice shelf, using model data, for the 2015/2016 melt season. Sections 3 and 5 provide evidence that the model is sufficiently accurate for this: it is quantitatively representative in terms of meteorology (Figure 2) and qualitatively representative in terms of SEB and melt (Figures 2 and 4) and how these relate to meteorological conditions (Figure 6). This model has also performed realistically in several previous studies (e.g., Elvidge et al., 2016, 2015; Orr et al., 2014). However, a significant and consistent overestimate in summertime radiatively driven surface warming and melt should be taken into consideration.

Figures 8–10 show model composite plots of key fields during *widespread foehn* and *widespread non-foehn* conditions across Larsen C. Here, *widespread foehn* is diagnosed when foehn is detected in the model (according to the criteria described in Appendix A) at both the Cabinet Inlet and Whirlwind Inlet sites. Likewise, *widespread non-foehn* conditions are diagnosed when foehn is occurring at neither of these sites in the model, while *limited foehn* conditions are diagnosed when foehn is detected at one inlet site but not the other. *Widespread foehn* is found to occur 12% of the time and is coincident with 20% of total Larsen C melt, while *widespread non-foehn* occurs 70% of the time and is coincident with 58% of the melt. This leaves *limited foehn* occurring 18% of the time and accounting for 22% of the melt. For simplicity, the *limited foehn* state is largely disregarded in this analysis and not shown in the figures. Note that while spatial plots of composite mean meteorological and surface conditions are provided for foehn conditions in Figure 8, equivalent

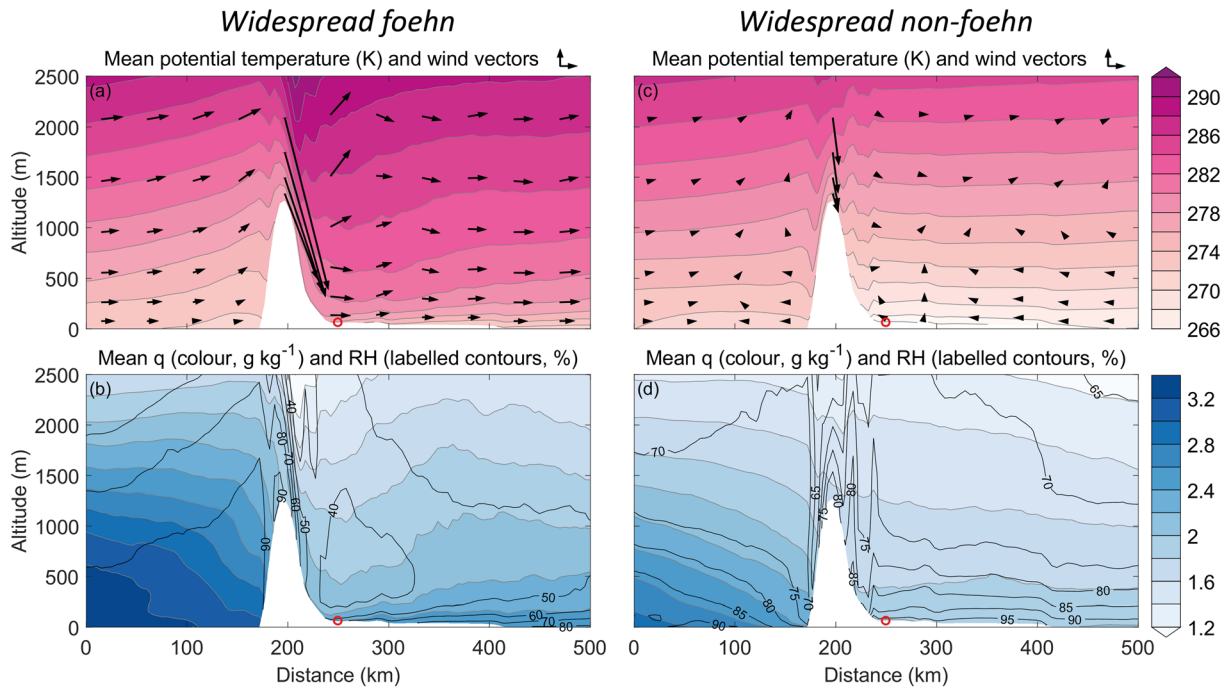

Figure 9. Model composite mean cross sections of (a, c) potential temperature (contours and shading) and winds vectors (arrows) and (b, d) specific humidity (q; shading) and relative humidity (RH; black contours) for (a, b) *widespread foehn* conditions (which occur 12% of the time) and (c, d) *widespread non-foehn* conditions (which occur 70% of the time) across the AP along the transect shown in Figure 8, for the 2015/2016 melt season. In these plots the vertical scale is exaggerated by a factor of 100 relative to the horizontal scale. The wind vectors are true to the aspect ratio used and the reference vectors (above plots) indicate 10 m s^{-1} horizontal winds and 0.1 m s^{-1} vertical winds. The red circle is the location of the Cabinet Inlet site.

plots are not shown for non-foehn conditions. This is due to non-foehn conditions being characterised by considerably greater variability in meteorology (limiting the usefulness of mean values) and much smaller spatial gradients in key variables across Larsen C.

Widespread foehn conditions are characterized in the composite mean by large-scale geostrophically forced westerly to northwesterly flow approaching and crossing the AP (Figures 8a and 8b). There is a clear foehn signature in the leeside response to these winds. In the immediate lee of the AP, a plunging flow signature is apparent in a cross section of composite mean wind vectors, associated with large cross-peninsula gradients in pressure, temperature, and humidity. Further downwind across the ice shelf, rising isentropes and specific humidity contours reflect the diminishing influence of foehn with distance downwind of the mountains (Figures 9a and 9b). Elvidge et al. (2016) demonstrated using case studies that the gradient of this diminishing influence depends on the linearity of the mountain flow regime in which the foehn is embedded. In very "nonlinear" cases, the impact of foehn on the leeside atmospheric boundary layer and ice shelf is confined to the foot of the mountains, while in the paths of jets in more "linear" cases the impact of foehn extends undiminished across the full width of the ice shelf (once the foehn is fully established in the boundary layer). Note that, with the foehn classification employed here, the distinction between these regimes is lost.

During *widespread foehn*, climatological foehn jets are apparent to the east of the AP, emerging from the mouths of major inlets (Figure 8b), as first observed and explained via case studies in Elvidge et al. (2015). The largest and strongest jet signatures are seen within and downwind of Cabinet Inlet and Whirlwind Inlet, while weaker jet signatures are seen within and downwind of Mill Inlet and the former Larsen B embayment. Everywhere across Larsen C, mean TurbH is downward and dominates over mean upward RadH (Figures 8c and 8d). The jet signatures correspond with the greatest TurbH fluxes and, consequently, the highest mean surface temperatures (Figure 8e). The standard deviation of surface temperature is smallest beneath the jets (Figure 8f), reflecting dampened (radiatively driven) diurnal and seasonal variability in surface temperature, due to a greater regulating influence of TurbH on surface temperature in these jet regions.

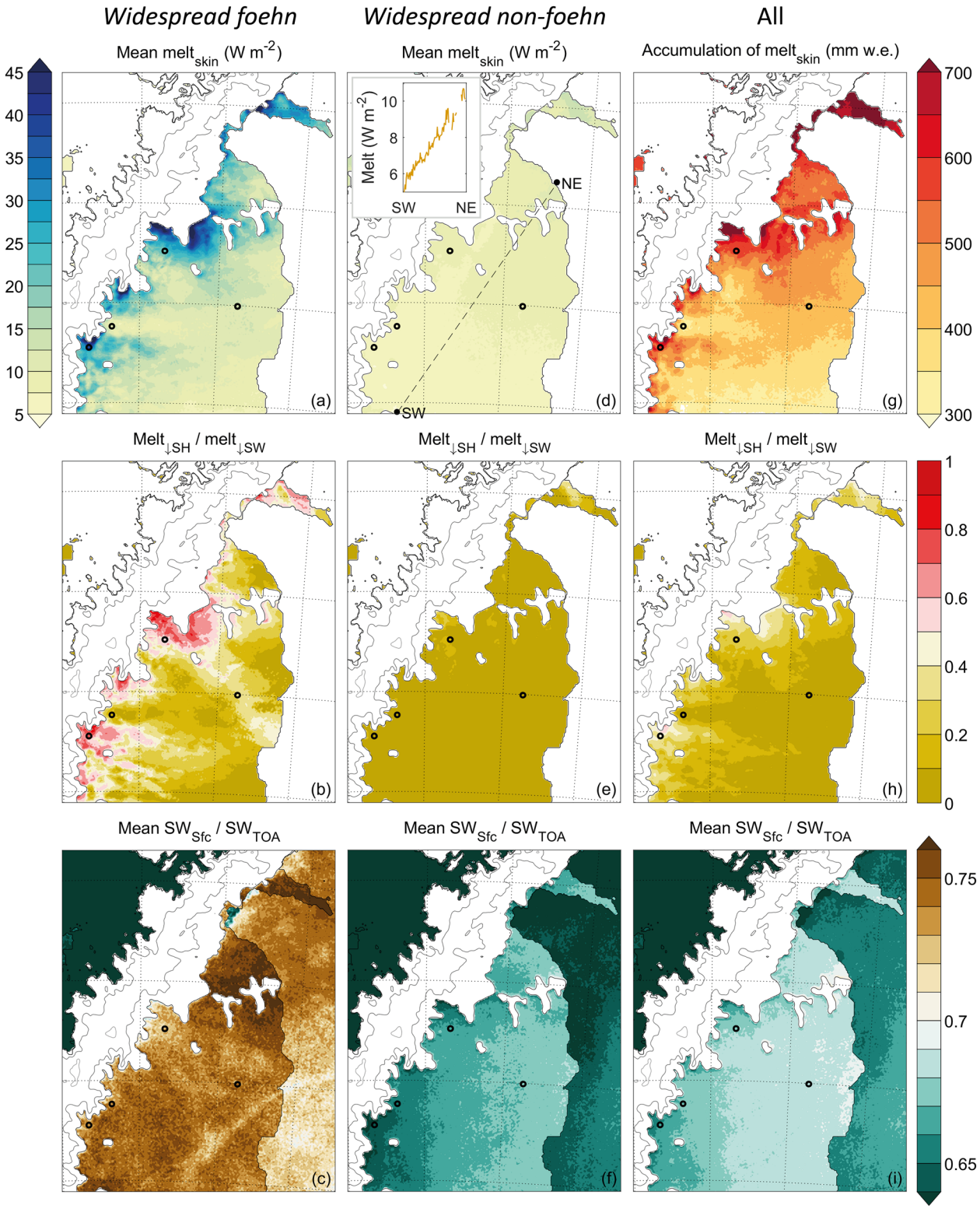

Figure 10. Model composite spatial plots during (a–c) *widespread foehn* (which occurs 12% of the time), (d–f) *widespread non-foehn* (which occurs 70% of the time), and (g–i) all conditions, for the 2015/2016 melt season. The fields shown are (a, d) mean melt$_{skin}$, (g) accumulation of melt$_{skin}$, (b, e, and h) the ratio of the accumulation of melt$_{skin}$ in the SEB$_{\downarrow SH}$ regime (melt$_{\downarrow SH}$) to that in the SEB$_{\downarrow SW}$ regime (melt$_{\downarrow SW}$), and (c, f, and i) the proportion of top of atmosphere solar irradiance reaching the surface (SW$_{Sfc}$/SW$_{TOA}$). Also shown, subset in (d), are mean melt rates during *widespread non-foehn* along the transect marked by the dashed line. Note that (a) and (d) use the color scale shown to the left of the plots. In each panel the locations of the four data sites are shown (open black circles; see Figure 1 for site names).

During *widespread foehn*, mean melt rates are relatively high and spatially variable across Larsen C (Figure 10a). The total ice-shelf-wide melt contributions by $SEB_{\downarrow SH}$ ($melt_{\downarrow SH}$) and $SEB_{\downarrow SW}$ ($melt_{\downarrow SW}$) are similar (50% each), though the spatial variability is almost entirely due to variability in $melt_{\downarrow SH}$ (see Figures 10a and 10b). Mean rates of $melt_{\downarrow SH}$ and consequently total melt broadly decline in a southeasterly direction, reflecting the mean northwesterly direction of foehn. This pattern also reflects the Cabinet Inlet jet being associated with the greatest and most widespread mean warming (consistent with the north-south gradient in the strength of the background circumpolar westerly winds; Marshall et al., 2006). The highest mean melt rates are found in the vicinity of the climatological foehn jets emerging from Cabinet Inlet, Whirlwind Inlet, and Mill Inlet, peaking at 66 W m^{-2} in the upper reaches of Cabinet Inlet. The majority of melt in these regions is due to $SEB_{\downarrow SH}$. The lowest melt rates are found at the eastern edge of the ice shelf, at the far south of the model domain (where an ice-shelf-wide minimum of 2 W m^{-2} is found), and within a strip of ice extending from Mamelon Point eastward. The majority of melt in these regions is due to $SEB_{\downarrow SW}$. Radiative contributions to melt during *widespread foehn* are enhanced via the cloud-clearance effect, which is evident across the entire ice shelf in terms of SW_{Sfc}/SW_{TOA} (cf. Figures 10c and 10f). Note that cloud cover is greatest in the upper reaches of Cabinet Inlet, consistent with leeside conditions being moistest in jets during foehn due to a dampened foehn drying effect here (see Elvidge et al., 2015). The lack of any foehn cloud-clearance seen in the Cabinet Inlet observations together with the model overestimate in SW here suggests the model underestimates the moisture in jets. It is interesting that, in contrast to SH (and $melt_{\downarrow SH}$; see Figures 10a and 10b), SW_{Sfc}/SW_{TOA} (and $melt_{\downarrow SW}$; not shown) does not diminish with distance downwind of the AP during foehn. This demonstrates that in the model the impact of foehn on the ice shelf extends beyond the reach of low-level foehn winds, due to cloud-clearance aloft.

During *widespread non-foehn* conditions, on average, cross-peninsula gradients in mean sea level pressure (MSLP) (not shown), temperature (Figure 9c) and relative humidity (Figure 9d) are the reverse of that during *widespread foehn*, and MSLP gradients and wind speeds are considerably weaker across the region. Over Larsen C, composite mean temperatures and specific humidities are considerably lower (by 7–12°C and ~0.6 g kg^{-1}, respectively) than during *widespread foehn*, while relative humidities are considerably higher (by 20–50%). This reflects the cool, southerly, continentally sourced air masses typical of non-foehn conditions, versus the warm, maritime character of the air masses which arrive from the west side of the AP to force foehn.

Melt during *widespread non-foehn* conditions occurs at much lower mean rates, is much less spatially variable than during *widespread foehn* (cf. Figures 10d and 10a) and is almost entirely (96%) due to $melt_{\downarrow SW}$ (Figure 10e). There is a weak northeast-southwest gradient in melt, with a maximum value of 11 W m^{-2} in the far northeast and a minimum value of 4 W m^{-2} in the far southwest (see inset transect in Figure 10d). This gradient reflects that of $melt_{\downarrow SW}$, which itself results from—in roughly equal contributions—latitudinal variability in incoming solar radiation and variability in cloud cover (indicated by SW_{Sfc}/SW_{TOA}; Figure 10f); see Appendix B. Although non-foehn winds most commonly have a southerly component, mean melt rates generally vary little with wind direction (not shown).

In total, much of the spatial variability in melt across Larsen C simulated during the 2015/2016 melt season is due to $melt_{\downarrow SH}$, governed by foehn. This is evident in the resemblance of the distribution of accumulated melt shown in Figure 10g with that in Figure 10a. Even so, the northeast-southwest gradient in melt seen during *widespread non-foehn* does—despite its weak signal in the mean—significantly impact the distribution of accumulated melt. $SEB_{\downarrow SW}$ contributes more melt than $SEB_{\downarrow SH}$ over the vast majority of the ice shelf and in total 79% of melt across Larsen C. This is due first to the predominance of non-foehn conditions, during which nearly all melt is driven by $SEB_{\downarrow SW}$, and second to the fact that, away from the inlets, $SEB_{\downarrow SW}$ also contributes significantly to melt during foehn conditions. In fact, as seen in the observations (see Figure 5b), the highest mean melt rates of any SEB regime are seen in $SEB_{\downarrow SW}$ during foehn; owing to secondary contributions by SH and, in the model, also due to cloud clearance.

In Figure 11, a more detailed analysis of SEB and melt characteristics is shown for Cabinet Inlet and the three additional sites (cf. Figure 1; Table 1). At these locations, foehn is diagnosed in a site-specific manner, as described in Appendix A. Across all four sites melt during foehn is more likely than melt during non-foehn conditions and occurs at greater rates. This is especially so at the two inlet sites, where the prevalence and relative impacts of the SEB regimes are qualitatively similar (Figures 11a–11d). At Whirlwind Inlet,

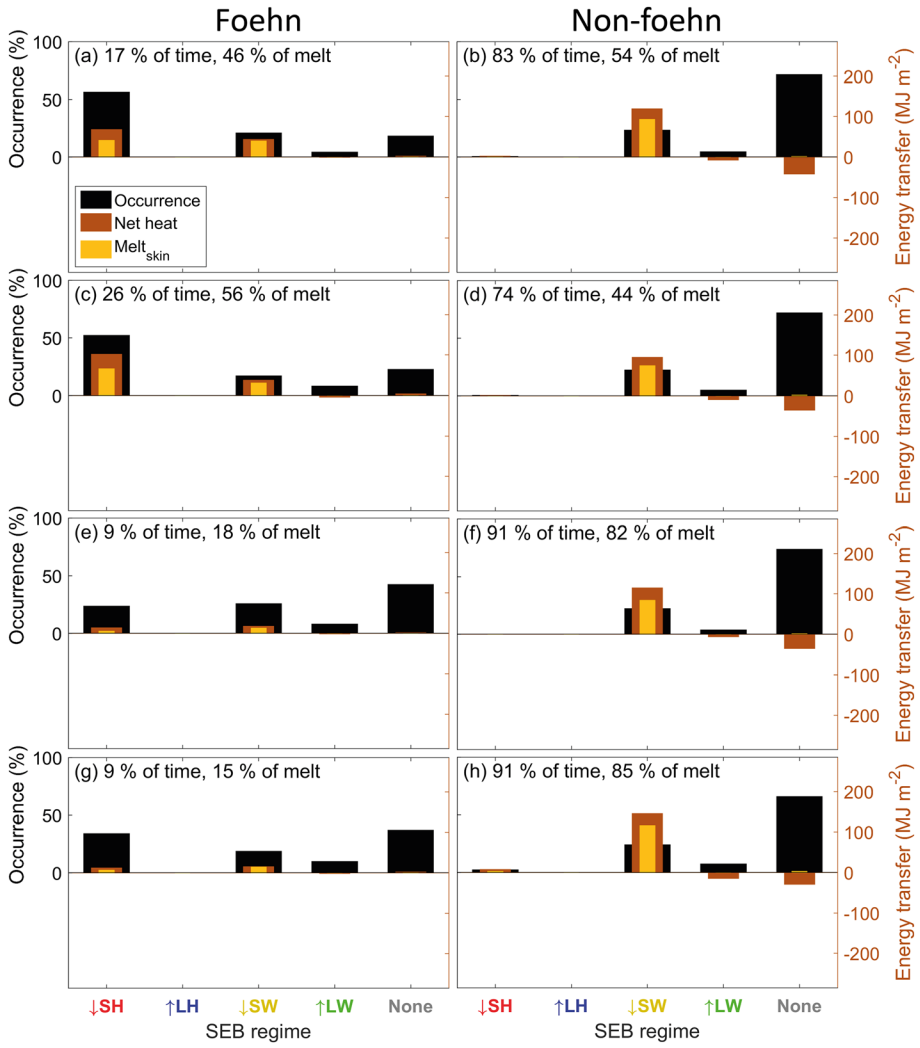

Figure 11. Prevalence and contributions to the SEB and melt of all SEB regimes, during (left) foehn and (right) non-foehn conditions from the model simulation at (a, b) the Cabinet Inlet site, (c, d) the Whirlwind Inlet site, (e, f) the Mamelon Point site, and (g, h) the Larsen East site. The black bars give the percentage of time during which each regime occurs and uses the left axis, while the brown and orange bars give cumulative contributions to net downward heat transfer and $melt_{skin}$ energy, respectively, and use the right axis. For each site the percentage of time spent and the percentage of $melt_{skin}$ generated in both foehn and non-foehn conditions are stated. The SEB regime "none" denotes where no single SEB component dominates (see text).

$SEB_{\downarrow SH}$ contributes slightly more melt, reflecting stronger mean foehn winds here than at Cabinet Inlet (Figure 8b).

At Larsen East and Mamelon Point, foehn occurs less frequently, owing to these locations being, respectively, ~150 km downwind of the AP and in a region known to typically experience wake conditions during foehn. When foehn does occur at these locations, it is associated with much less surface warming and melt (Figures 11e–11h). Both the prevalence and impact of $SEB_{\downarrow SH}$ are much lower, reflecting weaker foehn winds and, at Larsen East, lower foehn air temperatures. Of all four sites during foehn, $SEB_{\downarrow SH}$ is least common and $SEB_{\downarrow SW}$ most common at Mamelon Point. This is explained by its sheltered location, where foehn flows are typically very weak (Figure 8b) and dry (not shown), as explained in Elvidge et al. (2015). These particularly dry foehn conditions are associated with significantly higher SW_{Sfc}/SW_{TOA} than during non-foehn conditions, consistent with the cloud-clearance effect, which, of all four sites, is strongest here (Table 1). With distance downwind of the AP, spatial variability in mean foehn wind speed generally decreases as foehn jets broaden and weaken and wake regions disappear. This is reflected in $SEB_{\downarrow SH}$

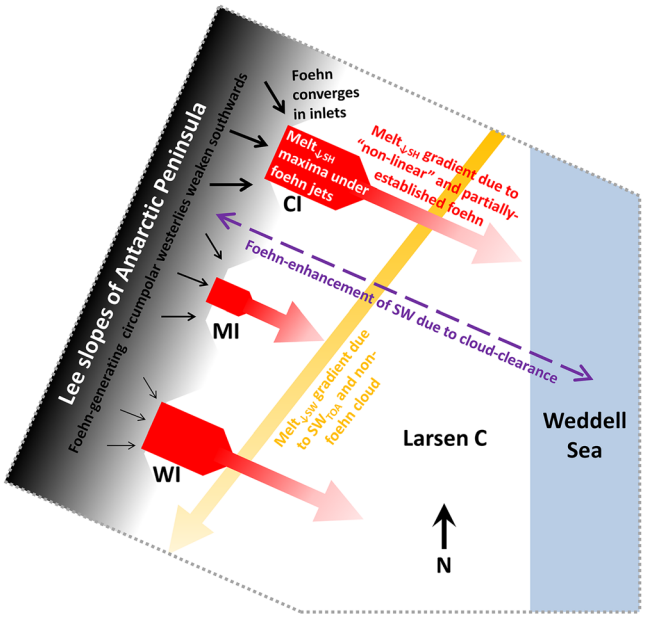

Figure 12. Schematic illustrating the key features of melt variability across Larsen C, and the meteorological conditions responsible for them. Note that "nonlinear" foehn refers to foehn embedded in a nonlinear mountain flow regime (see Elvidge et al., 2016) and that while the cloud-clearance effect is evident in the model results across the entire ice shelf, is it not evident in the observations at Cabinet Inlet. The inlets are labeled CI, MI, and WI; Cabinet Inlet, Mill Inlet, and Whirlwind Inlet, respectively.

being more common at Larsen East, which experiences on average stronger foehn winds than Mamelon Point. During non-foehn conditions, there is comparatively little variation between the four sites in terms of the prevalence and impact of SEB regimes, with slight variability in the degree of warming and melt reflecting the northeast-southwest gradient in $SEB_{\downarrow SW}$ described above.

The simulated spatial melt patterns described in this section closely resemble those seen in the satellite observations of Bevan et al. (2018) for an annual period encompassing the same melt season (2015/2016), which in turn are typical of melt distributions observed during other recent melt seasons (e.g., Bevan et al., 2018; Luckman et al., 2014). The north-south gradient in satellite-observed melt is reproduced and shown to be due to a combination of a northeast-southwest gradient in mean $melt_{\downarrow SW}$ during non-foehn conditions and a broadly northwest to southeast mean gradient in $melt_{\downarrow SH}$ during foehn (in nonlinear mountain flow regimes and boundary layers in which the foehn has yet to fully establish). Also reproduced is the observed band of generally high melt rates along the AP's east coast, in particular in the inlets (e.g., Figure 10g). This is demonstrated to be due to the foehn winds here being generally stronger, resulting in greater SH-driven melt. In the inlets, more frequent foehn occurrence also contributes to more cumulative melt. Beyond these generally well-captured broad-scale features, there are regional discrepancies. Most notably, the simulated melt deficit around Mamelon Point relative to neighboring inlets appears to be exaggerated compared to observations (cf. Bevan et al., 2018). However, another wake region and melt minimum in the model—between Mill Inlet and Cabinet Inlet—is consistent with observations. Figure 12 summarizes in schematic form the key patterns in Larsen C melt discussed here and the mechanisms which we have found to be responsible for them.

7. Discussion and Conclusions

This study has employed the first set of observations from a Larsen C inlet, in conjunction with a season-long, high-resolution simulation in a state-of-the-art model (the MetUM) to provide the first comprehensive explanation of patterns in SEB and melt across Larsen C. A novel approach to classifying the SEB regime according to the *dominant* SEB component has afforded a useful means of attributing variability in net SEB and melt to atmospheric drivers.

The climatological impact of foehn on the Larsen C SEB is distinct and significant, with elevated occurrences and rates of melt, especially in inlets. During 31 months of observations at Cabinet Inlet, foehn contributes 45% of total melt despite only occurring 15% of the time. During foehn, melt occurs 3 times more often and, when it does occur, it does so at a rate greater by a factor of 1.4. Foehn melt accounts for nearly 90% of melt observed outside the summer months (DJF), virtually all of which takes place during spring (SON; during which foehn is also likely to play an important role in the preconditioning of the ice shelf for summertime melt) and autumn (MAM). In the model, comparable statistics are simulated for inlets and even in regions where the net impact of foehn is weakest (in the southeast and in wake regions). Owing to sharp gradients in mean melt, foehn governs the spatial distribution in cumulative melt simulated across Larsen C for the 2015/2016 melt season.

While foehn is the more potent agent of melt, non-foehn conditions occur much more commonly and contribute more melt than foehn everywhere across Larsen C outside of the inlets. Nearly all non-foehn-driven melt is due to SW during the summer months (90% occurring during DJF in the Cabinet Inlet observations). Non-foehn-driven melt varies comparatively little in the mean across Larsen C. However, a subtle northeast to southwest gradient reflects a corresponding gradient in surface solar forcing, resulting from spatial variability in both top-of-atmosphere solar irradiance and cloud cover; this is significant to the distribution of total cumulative melt. The hemisphere- and synoptic-scale circulation patterns governing non-foehn driven melt is a subject for future research.

Many previous studies, both over Larsen C (e.g., Grosvenor et al., 2014; King et al., 2017; Kuipers Munneke et al., 2012) and elsewhere in the world (e.g. over John Evans Glacier, Canada; Boon et al., 2003; on Hokkaido Island, Japan, Hayashi et al., 2005; over the Baltic Sea, Granskog et al., 2006; and in Southern Alberta, Canada, MacDonald et al., 2018), have found the impact of foehn on snow and ice melt to be largely limited to elevated contributions by downward SW (due to a cancelation of SH by LH). In contrast, our results show that the primary impact of foehn over Larsen C is elevated contributions to melt by downward SH. This finding is consistent with the case study results of Elvidge et al. (2016) and Kuipers Munneke et al. (2018). The majority (76% in our observations) of foehn-driven melt occurs when SH dominates the SEB as a result of strong, warm foehn winds passing over a much cooler ice surface. The majority of such melt (and roughly half of total foehn-driven melt) occurs in the absence of solar forcing, during the night or outside the summer season. However, SW does significantly contribute to foehn-driven melt, with most of the remaining melt (19%) occurring when SW dominates the SEB regime. During such conditions, SH typically also contributes, leading to the highest melt rates observed at Cabinet Inlet. In the model, foehn enhancement of SW is evident across the entire ice shelf, reflecting widespread cloud clearance. However, this enhancement is not apparent in the Cabinet Inlet observations. The foehn cloud-clearance effect has previously been inferred from both observations and model output at Larsen East during the 2010/2011 summer season (King et al., 2017; Kuipers Munneke et al., 2012), but the effect was small and not statistically significant. Further work is required to establish the significance of this effect over Larsen C more generally.

Satellite observations across Larsen C have demonstrated that the foehn-jet-prone inlets experience the most cumulative melt (e.g., Bevan et al., 2018; Luckman et al., 2014). However, previous case study simulations have been unable to reproduce this melt pattern (e.g., Elvidge, 2013; Grosvenor et al., 2014). We now know why: the impact of foehn is critically sensitive to wind strength, the influence of which is modulated by the warmth of incoming foehn relative to the ice surface, via the turbulent heat fluxes. Typical foehn is much warmer than the ice and results in the highest melt rates occurring beneath the strongest foehn winds (i.e., in the inlets), where downward SH is greatest. Less commonly, cooler foehn winds result in the highest melt rates occurring beneath the weakest foehn winds (i.e., in wakes), where upward LH is smallest. This more unusual *weakly stratified foehn* state occurs 5% of the time in the Cabinet Inlet observations and is associated with small air-ice temperature gradients and typically sunny conditions. It accounts for the incidence of melt minima beneath jets in such cases as that examined by Elvidge (2013).

Another notable finding of this study is the signature of a foehn jet in simulated mean wind speed passing over the embayment formerly occupied by the Larsen B Ice Shelf (until its collapse in 2002). This jet is associated with elevated SH-driven surface warming and is also seen in the multidecadal simulation data presented in Wiesenekker et al. (2018). Whether this jet exists in reality and whether it was common prior to the collapse of Larsen B is unknown and could be a focus of future work.

The MetUM has been shown to provide a quantitatively accurate representation of the occurrence of foehn and annual melt and to provide a qualitatively accurate representation of SEB and melt variability during the 2015/2016 melt season at Cabinet Inlet. Furthermore, the modeled spatial distribution of cumulative melt across Larsen C corresponds remarkably well with satellite observations of melt during the same melt season (see Bevan et al., 2018), which is typical of melt distributions observed during other melt seasons. This provides confidence that our model results are realistic and useful. The broad, roughly north-south gradient in melt seen in observations is reproduced and shown to be due to a combination of the aforementioned northeast to southwest gradient in SW-driven melt during non-foehn conditions, and a northwest to southeast gradient in SH-driven melt in foehn conditions (due to "nonlinear" cross-peninsula flow; Elvidge et al., 2016). Also reproduced is the observed band of generally high melt rates along the AP's east coast, in particular in the inlets. The prior assumption that this is due to the impact of foehn (and consequently SH-driven melt) is confirmed. Despite the model's successes, there is a consistent and significant positive bias in SW, which is consistent with the findings of previous studies with the same and different models (e.g., Gilbert et al., 2020; Grosvenor et al., 2014; King et al., 2015; Kirchgaessner et al., 2019). This bias results in significant overestimates in melt during the summer months, particularly during non-foehn conditions, and implies deficiencies in the model's representation of clouds and/or surface albedo (in the MetUM, largely clouds; Gilbert et al., 2020).

Our study demonstrates that the accuracy of model simulations of Larsen C melt depends critically on the accurate reproduction of (a) summertime incoming SW at the surface (and consequently clouds and albedo), (b) the occurrence, strength and warmth of foehn winds at the surface, and (c) air-ice boundary layer coupling and consequently the balance between SH and LH fluxes during foehn. These are all known to be challenging processes for models, though in recent years there has been some notable progress. For example, it has recently been shown that significant improvements in the representation of the supercooled liquid phase in Antarctic clouds are possible with the adoption of a realistic double-moment ice cloud microphysics scheme (Listowski & Lachlan-Cope, 2017). Recent developments in the dynamical cores around which atmospheric models are built have also significantly improved the capacity of models to resolve the gravity waves and flow perturbations (of which foehn is an example) induced by mountains (Elvidge et al., 2017). However, melt ponds—known to significantly affect the SEB and melt on Larsen C (Buzzard et al., 2018a.b)—remain notably missing from numerical models of the cryosphere.

The degree to which Larsen C is in equilibrium with present-day atmospheric forcing is unclear. Furthermore, future changes in this forcing are expected. For example, the index of the Southern Annular Mode (SAM), which governs the strength of the prevailing westerly winds across the AP, is expected to vary in accordance with future greenhouse gas emissions (Abram et al., 2014). Any future positive trend in the SAM index, as predicted in high emission scenarios of the Coupled Model Intercomparison Project Phase 5 (CMIP5) projections (Zheng et al., 2013), would likely yield a greater-still influence of foehn on Larsen C. Changes in the atmospheric forcing may also be instigated by changes in the cryosphere itself—for example, calving events and sea ice decline. Our ability to predict such changes and consequently the ice shelf's future stability relies on underpinning mechanistic understanding of the complex interactions at the atmosphere-cryosphere interface (such as provided by the present study), the coverage of strategically located observational platforms in the region (such as the Cabinet Inlet AWS), and on the capability of atmosphere-cryosphere coupled climate models.

Appendix A: Foehn Detection

The algorithmic classification of foehn is a nontrivial matter, for which there is no established best practice (Mayr et al., 2018). In this study, a comparatively simple approach has been adopted, based on the assumption that foehn has a sufficiently distinct and temporally invariant signature at a given location to be identified in situ using simple fixed thresholds of key meteorological fields in absolute terms (i.e., not relative to pre-foehn or post-foehn conditions). This assumption is supported by climatological analysis of the AWS data (not shown) and by the findings of Turton et al. (2018), Kuipers Munneke et al. (2018), and King et al. (2017). Accordingly, we have used only leeside near-surface data and employ thresholds in wind direction and relative humidity, which vary on a site-by-site basis, according to (a) location with respect to the upwind orography and (b) analysis of selected cases studies. For the Cabinet Inlet site (observations and model) and the Whirlwind Inlet site (model only), foehn conditions have been defined by wind directions being between southwesterly and northerly and the relative humidity with respect to ice (hereafter simply "relative humidity") being below 75%. This threshold has been chosen based on case study analysis of AWS and model data to afford detection of the great majority of foehn cases while excluding other

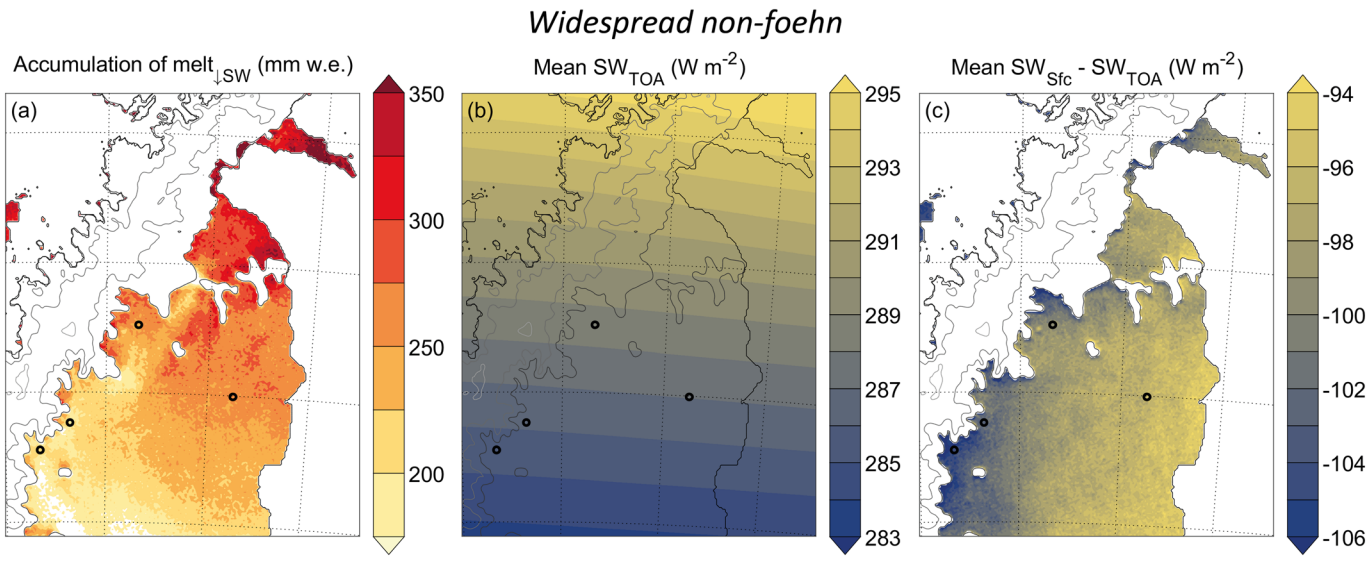

Figure B1. (a) The accumulation of melt in the $SEB_{\downarrow SW}$ regime ($melt_{\downarrow SW}$), and (b,c) contributions to the downward component of SW at the surface (SW_{Sfc}) by (b) top of atmosphere solar irradiance (SW_{TOA}) and (c) blocking of SW by clouds (expressed here as $SW_{Sfc} - SW_{TOA}$; smaller negative values indicating clearer conditions), all during non-foehn conditions. Note that the color scales used for panels (b) and (c) cover an identical range of values, facilitating direct comparisons of the gradients in these fields.

westerly flows at Cabinet Inlet, for example, barrier winds and katabatic winds (e.g., Grazioli et al., 2017). Despite the cross-mountain foehn drying effect, the maritime influence on circumpolar westerlies means that foehn air over Larsen C is not necessarily comparatively dry in terms of absolute humidity. However, the warmth of foehn air means it can typically hold much more water vapor than the typically cool air sourced from east of the AP (including barrier winds) or the mountains (including katabatic winds).

For the Mamelon Point (model only) site, foehn is diagnosed when relative humidity is below 75% and foehn is diagnosed at one or both of the two inlet sites. The rationale for this is that the foehn wake conditions known to occur at the Mamelon Point site are typically characterized by near-stagnant flow and recirculated foehn air (Elvidge et al., 2015), rendering a wind direction criterion inappropriate. However, given the close proximity to the AP, the same relative humidity criterion as used for the two inlets is appropriate. The fact that foehn occurrence in a wake region is unlikely without foehn occurrence in nearby inlets (into which foehn is preferentially funneled; Elvidge et al., 2015) justifies the additional condition that foehn must be occurring in at least one of the two inlet sites.

For the Larsen East (model only) site, the detection criterion has been designed to account for its distance from the AP. Here, foehn is diagnosed when relative humidity is below 80% and either of the following two conditions is met:

1. Wind direction at Larsen East is between westerly and north-northwesterly, and foehn is diagnosed at Cabinet Inlet;
2. Wind direction at Larsen East is between west-southwesterly and westerly, and foehn is diagnosed at Whirlwind Inlet.

The relative humidity threshold of 80% has been inferred from the model data, being an estimate of the average relative humidity of air arriving at Larsen East from one of the inlets having had a relative humidity of 75% in the inlet.

Appendix B: Figure B1 shows that the latitudinal gradient in SW_{TOA} and spatial variability in cloud cover are roughly equally responsible for the spatial variability in accumulative $melt_{\downarrow sfc}$ across Larsen C during non-foehn conditions.

Data Availability Statement

The AWS19 observational data used in this study is available in Bevan et al. (2020). The model data were derived from a Met Office Unified Model simulation carried out on the Joint Weather and Climate

Research Programme (Met Office and NERC) MONSooN computing system. These data require a large tape storage facility and have been archived through the Met Office mass storage system, accessible through the STFC-CEDA platform JASMIN (Lawrence et al., 2013).

Acknowledgments
This paper was made possible by funding provided by NERC under the Project Grant NE/N009754/1. P. Kuipers Munneke acknowledges funding from the Netherlands Earth System Science Centre. The British Antarctic Survey (BAS) is acknowledged for the servicing of the automatic weather station in Cabinet Inlet (AWS18), and for the archiving of the AWS18 data. We thank Tony Phillips at BAS for his assistance in preparing the land-sea mask and orography data used for the model simulation, and Sam Nair at The QK Institute for advice on graphical representation.

References

Abram, N. J., Mulvaney, R., Vimeux, F., Phipps, S. J., Turner, J., & England, M. H. (2014). Evolution of the Southern Annular Mode during the past millennium. *Nature Climate Change*, *4*(7), 564–569. https://doi.org/10.1038/nclimate2235

Ashmore, D. W., Hubbard, B., Luckman, A., Kulessa, B., Bevan, S., Booth, A., et al. (2017). Ice and firn heterogeneity within Larsen C Ice Shelf from borehole optical televiewing. *Journal of Geophysical Research: Earth Surface*, *122*, 1139–1153. https://doi.org/10.1002/2016JF004047

Barrand, N. E., Vaughan, D. G., Steiner, N., Tedesco, M., Kuipers Munneke, P., Van den Broeke, M. R., & Hosking, J. S. (2013). Trends in Antarctic Peninsula surface melting conditions from observations and regional climate modeling. *Journal of Geophysical Research: Earth Surface*, *118*, 315–330. https://doi.org/10.1029/2012JF002559

Bevan, S. L., Luckman, A. J., Kuipers Munneke, P., Hubbard, B., Kulessa, B., & Ashmore, D. W. (2018). Decline in surface melt duration on Larsen C ice shelf revealed by the Advanced Scatterometer (ASCAT). *Earth and Space Science*, *5*, 578–591. https://doi.org/10.1029/2018EA000421

Boon, S., Sharp, M., & Nienow, P. (2003). Impact of an extreme melt event on the runoff and hydrology of a high Arctic glacier. *Hydrological Processes*, *17*(6), 1051–1072. https://doi.org/10.1002/hyp.1194

Buzzard, S. C., Feltham, D. L., & Flocco, D. (2018a). A mathematical model of melt lake development on an ice shelf. *Journal of Advances in Modeling Earth Systems*, *10*(2), 262–283.

Buzzard, S., Feltham, D., & Flocco, D. (2018b). Modelling the fate of surface melt on the Larsen C Ice Shelf. *Cryosphere*, *12*(11), 3565–3575.

Cape, M. R., Vernet, M., Skvarca, P., Marinsek, S., Scambos, T., & Domack, E. (2015). Foehn winds link climate-driven warming to ice shelf evolution in Antarctica. *Journal of Geophysical Research: Atmospheres*, *120*, 11,037–11,057. 10.1002/2015JD023465

Cook, A. J., & Vaughan, D. G. (2010). Overview of areal changes of the ice shelves on the Antarctic Peninsula over the past 50 years. *The Cryosphere*, *4*(1), 77–98. https://doi.org/10.5194/tc-4-77-2010

Datta, R. T., Tedesco, M., Fettweis, X., Agosta, C., Lhermitte, S., Lenaerts, J., & Wever, N. (2019). The effect of foehn-induced surface melt on firn evolution over the northeast Antarctic Peninsula. *Geophysical Research Letters*, *46*, 3822–3831. https://doi.org/10.1029/2018GL080845

Elvidge, A. (2013). Polar föhn winds and warming over the Larsen C Ice Shelf, Antarctica (Doctoral dissertation, University of East Anglia).

Elvidge, A. D., & Renfrew, I. A. (2016). The causes of foehn warming in the lee of mountains. *Bulletin of the American Meteorological Society*, *97*(3), 455–466. https://doi.org/10.1175/BAMS-D-14-00194.1

Elvidge, A. D., Renfrew, I. A., King, J. C., Orr, A., & Lachlan-Cope, T. A. (2016). Foehn warming distributions in nonlinear and linear flow regimes: A focus on the Antarctic Peninsula. *Quarterly Journal of the Royal Meteorological Society*, *142*(695), 618–631. https://doi.org/10.1002/qj.2489

Elvidge, A. D., Renfrew, I. A., King, J. C., Orr, A., Lachlan-Cope, T. A., Weeks, M., & Gray, S. L. (2015). Foehn jets over the Larsen C ice shelf, Antarctica. *Quarterly Journal of the Royal Meteorological Society*, *141*(688), 698–713. https://doi.org/10.1002/qj.2382

Elvidge, A. D., Vosper, S. B., Wells, H., Cheung, J. C., Derbyshire, S. H., & Turp, D. (2017). Moving towards a wave-resolved approach to forecasting mountain wave induced clear air turbulence. *Meteorological Applications*, *24*(3), 540–550. https://doi.org/10.1002/met.1656

Gilbert, E., Orr, A., King, J. C., Renfrew, I. A., Lachlan-Cope, T., Field, P. F., & Boutle, I. A. (2020). Summertime cloud phase strongly influences surface melting on the Larsen C ice shelf, Antarctica. *Quarterly Journal of the Royal Meteorological Society*, *146*, 1575–1589. https://doi.org/10.1002/qj.3753

Granskog, M. A., Vihma, T., Pirazzini, R., & Cheng, B. (2006). Superimposed ice formation and surface energy fluxes on sea ice during the spring melt–freeze period in the Baltic Sea. *Journal of Glaciology*, *52*(176), 119–127. https://doi.org/10.3189/172756506781828971

Grazioli, J., Madeleine, J. B., Gallée, H., Forbes, R. M., Genthon, C., Krinner, G., & Berne, A. (2017). Katabatic winds diminish precipitation contribution to the Antarctic ice mass balance. *Proceedings of the National Academy of Sciences*, *114*(41), 10,858–10,863. https://doi.org/10.1073/pnas.1707633114

Grosvenor, D. P., King, J. C., Choularton, T. W., & Lachlan-Cope, T. (2014). Downslope föhn winds over the Antarctic Peninsula and their effect on the Larsen ice shelves. *Atmospheric Chemistry and Physics*, *14*(18), 9481–9509. https://doi.org/10.5194/acp-14-9481-2014

Hayashi, M., Hirota, T., Iwata, Y., & Takayabu, I. (2005). Snowmelt energy balance and its relation to foehn events in Tokachi, Japan. *Journal of the Meteorological Society of Japan. Series II*, *83*(5), 783–798.

Holland, P. R., Corr, H. F., Pritchard, H. D., Vaughan, D. G., Arthern, R. J., Jenkins, A., & Tedesco, M. (2011). The air content of Larsen Ice Shelf. *Geophysical Research Letters*, *38*, L10503. https://doi.org/10.1029/2011GL047245

Hubbard, B., Luckman, A., Ashmore, D. W., Bevan, S., Kulessa, B., Munneke, P. K., et al. (2016). Massive subsurface ice formed by refreezing of ice-shelf melt ponds. *Nature Communications*, *7*(1), 11,897. https://doi.org/10.1038/ncomms11897

King, J. C., Gadian, A., Kirchgaessner, A., Kuipers Munneke, P., Lachlan-Cope, T. A., Orr, A., et al. (2015). Validation of the summertime surface energy budget of Larsen C Ice Shelf (Antarctica) as represented in three high-resolution atmospheric models. *Journal of Geophysical Research: Atmospheres*, *120*, 1335–1347. https://doi.org/10.1002/2014JD022604

King, J. C., Kirchgaessner, A., Bevan, S., Elvidge, A. D., Kuipers Munneke, P., Luckman, A., et al. (2017). The impact of föhn winds on surface energy balance during the 2010–2011 melt season over Larsen C Ice Shelf, Antarctica. *Journal of Geophysical Research: Atmospheres*, *122*, 12,062–12,076. https://doi.org/10.1002/2017JD026809

King, J. C., Lachlan-Cope, T. A., Ladkin, R. S., & Weiss, A. (2008). Airborne measurements in the stable boundary layer over the Larsen Ice Shelf, Antarctica. *Boundary-Layer Meteorology*, *127*(3), 413.

Kirchgaessner, A., King, J., & Gadian, A. (2019). The representation of Föhn events to the east of the Antarctic Peninsula in simulations by the Antarctic Mesoscale Prediction System (AMPS). *Journal of Geophysical Research: Atmospheres*, *124*, 13,663–13,679. https://doi.org/10.1029/2019JD030637

Kuipers Munneke, P., Ligtenberg, S. R., Van den Broeke, M. R., & Vaughan, D. G. (2014). Firn air depletion as a precursor of Antarctic ice-shelf collapse. *Journal of Glaciology*, *60*(220), 205–214. https://doi.org/10.3189/2014JoG13J183

Kuipers Munneke, P., Luckman, A. J., Bevan, S. L., Smeets, C. J. P. P., Gilbert, E., Van Den Broeke, M. R., et al. (2018). Intense winter surface melt on an Antarctic ice shelf. *Geophysical Research Letters*, *45*, 7615–7623. https://doi.org/10.1029/2018GL077899

Kuipers Munneke, P., Van den Broeke, M. R., King, J. C., Gray, T., & Reijmer, C. H. (2012). Near-surface climate and surface energy budget of Larsen C ice shelf, Antarctic Peninsula. *The Cryosphere*, *6*(2), 353–363. https://doi.org/10.5194/tc-6-353-2012

Kuipers Munneke, P., Van den Broeke, M. R., Reijmer, C. H., Helsen, M. M., Boot, W., Schneebeli, M., & Steffen, K. (2009). The role of radiation penetration in the energy budget of the snowpack at Summit, Greenland. *The Cryosphere*, *3*(2), 155–165. https://doi.org/10.5194/tc-3-155-2009

Larsen, C. A. (1894). The voyage of the "Jason" to the Antarctic regions. *The Geographical Journal*, *4*(4), 333–344. https://doi.org/10.2307/1773537

Lawrence, B.N., Bennett, V.L., Churchill, J., Juckes, M., Kershaw, P., Pascoe, S., et al. (2013). October. Storing and manipulating environmental big data with JASMIN. In 2013 IEEE international conference on big data (pp. 68-75). IEEE.

Leeson, A. A., Van Wessem, J. M., Ligtenberg, S. R. M., Shepherd, A., Van den Broeke, M. R., Killick, R., et al. (2017). Regional climate of the Larsen B embayment 1980–2014. *Journal of Glaciology*, *63*(240), 683–690. https://doi.org/10.1017/jog.2017.39

Listowski, C., & Lachlan-Cope, T. (2017). The microphysics of clouds over the Antarctic Peninsula—Part 2: Modelling aspects within Polar WRF. *Atmospheric Chemistry and Physics*, *17*(17), 10,195–10,221. https://doi.org/10.5194/acp-17-10195-2017

Liu, H., Jezek, K. C., Li, B., & Zhao, Z. (2015). Radarsat Antarctic Mapping Project Digital Elevation Model, Version 2. Boulder, Colorado USA. NASA National Snow and Ice Data Center Distributed Active Archive Center. https://doi.org/10.5067/8JKNEW6BFRVD. [Accessed March 2017].

Luckman, A., Elvidge, A., Jansen, D., Kulessa, B., Munneke, P. K., King, J., & Barrand, N. E. (2014). Surface melt and ponding on Larsen C Ice Shelf and the impact of föhn winds. *Antarctic Science*, *26*(6), 625–635. https://doi.org/10.1017/S0954102014000339

MacDonald, M. K., Pomeroy, J. W., & Essery, R. L. (2018). Water and energy fluxes over northern prairies as affected by Chinook winds and winter precipitation. *Agricultural and Forest Meteorology*, *248*, 372–385. https://doi.org/10.1016/j.agrformet.2017.10.025

Marshall, G. J., Orr, A., Van Lipzig, N. P., & King, J. C. (2006). The impact of a changing Southern Hemisphere Annular Mode on Antarctic Peninsula summer temperatures. *Journal of Climate*, *19*(20), 5388–5404. https://doi.org/10.1175/JCLI3844.1

Mayr, G. J., Armi, L., Gohm, A., Zängl, G., Durran, D. R., Flamant, C., et al. (2007). Gap flows: Results from the Mesoscale Alpine Programme. *Quarterly Journal of the Royal Meteorological Society*, *133*(625), 881–896. https://doi.org/10.1002/qj.66

Mayr, G. J., Plavcan, D., Armi, L., Elvidge, A., Grisogono, B., Horvath, K., et al. (2018). The community foehn classification experiment. *Bulletin of the American Meteorological Society*, *99*(11), 2229–2235. https://doi.org/10.1175/BAMS-D-17-0200.1

Morris, E. M., & Vaughan, D. G. (2003). Spatial and temporal variation of surface temperature on the Antarctic Peninsula and the limit of viability of ice shelves. *Antarctic Peninsula Climate Variability: Historical and Paleoenvironmental Perspectives*, *79*, 61–68.

Orr, A., Marshall, G. J., Hunt, J. C., Sommeria, J., Wang, C. G., Van Lipzig, N. P., et al. (2008). Characteristics of summer airflow over the Antarctic Peninsula in response to recent strengthening of westerly circumpolar winds. *Journal of the Atmospheric Sciences*, *65*(4), 1396–1413. https://doi.org/10.1175/2007JAS2498.1

Orr, A., Phillips, T., Webster, S., Elvidge, A., Weeks, M., Hosking, S., & Turner, J. (2014). Met Office Unified Model high-resolution simulations of a strong wind event in Antarctica. *Quarterly Journal of the Royal Meteorological Society*, *140*(684), 2287–2297. https://doi.org/10.1002/qj.2296

Parish, T. R. (1983). The influence of the Antarctic Peninsula on the wind field over the western Weddell Sea. *Journal of Geophysical Research*, *88*(C4), 2684–2692. https://doi.org/10.1029/JC088iC04p02684

Scambos, T. A., Hulbe, C., Fahnestock, M., & Bohlander, J. (2000). The link between climate warming and break-up of ice shelves in the Antarctic peninsula. *Journal of Glaciology*, *46*(154), 516–530. https://doi.org/10.3189/172756500781833043

Schwerdtfeger, W. (1975). The effect of the Antarctic Peninsula on the temperature regime of the Weddell Sea. *Monthly Weather Review*, *103*(1), 45–51. https://doi.org/10.1175/1520-0493(1975)103%3C0045:TEOTAP%3E2.0.CO;2

Smeets, P. C., Kuipers Munneke, P., Van As, D., van den Broeke, M. R., Boot, W., Oerlemans, H., et al. (2018). The K-transect in West Greenland: Automatic weather station data (1993–2016). *Arctic, Antarctic, and Alpine Research*, *50*(1), S100002.

Tang, Y., Lean, H. W., & Bornemann, J. (2013). The benefits of the Met Office variable resolution NWP model for forecasting convection. *Meteorological Applications*, *20*(4), 417–426. https://doi.org/10.1002/met.1300

Tedesco, M. (2009). Assessment and development of snowmelt retrieval algorithms over Antarctica from K-band spaceborne brightness temperature (1979–2008). *Remote Sensing of Environment*, *113*(5), 979–997. https://doi.org/10.1016/j.rse.2009.01.009

Turton, J. V., Kirchgaessner, A., Ross, A. N., & King, J. C. (2017). Does high-resolution modelling improve the spatial analysis of föhn flow over the Larsen C Ice Shelf? *Weather*, *72*(7), 192–196. https://doi.org/10.1002/wea.3028

Turton, J. V., Kirchgaessner, A., Ross, A. N., & King, J. C. (2018). The spatial distribution and temporal variability of föhn winds over the Larsen C Ice Shelf, Antarctica. *Quarterly Journal of the Royal Meteorological Society*, *144*(713), 1169–1178. https://doi.org/10.1002/qj.3284

Valisuo, I., Vihma, T., & King, J. C. (2014). Surface energy budget on Larsen and Wilkins ice shelves in the Antarctic Peninsula: Results based on reanalyses in 1989–2010. *The Cryosphere*, *8*(4), 1519–1538. https://doi.org/10.5194/tc-8-1519-2014

van den Broeke, M. (2005). Strong surface melting preceded collapse of Antarctic Peninsula ice shelf. *Geophysical Research Letters*, *32*, L12815. https://doi.org/10.1029/2005GL023247

Van den Broeke, M., van As, D., Reijmer, C., & van de Wal, R. (2004). Assessing and improving the quality of unattended radiation observations in Antarctica. *Journal of Atmospheric and Oceanic Technology*, *21*(9), 1417–1431. https://doi.org/10.1175/1520-0426(2004)021%3C1417:AAITQO%3E2.0.CO;2

Van den Broeke, M., Van As, D., Reijmer, C., & Van de Wal, R. (2005). Sensible heat exchange at the Antarctic snow surface: A study with automatic weather stations. *International Journal of Climatology: A Journal of the Royal Meteorological Society*, *25*(8), 1081–1101. https://doi.org/10.1002/joc.1152

Van Lipzig, N. P., Marshall, G. J., Orr, A., & King, J. C. (2008). The relationship between the Southern Hemisphere Annular Mode and Antarctic Peninsula summer temperatures: Analysis of a high-resolution model climatology. *Journal of Climate*, *21*(8), 1649–1668. https://doi.org/10.1175/2007JCLI1695.1

Vaughan, D. G., & Doake, C. S. M. (1996). Recent atmospheric warming and retreat of ice shelves on the Antarctic Peninsula. *Nature*, *379*(6563), 328–331. https://doi.org/10.1038/379328a0

Walters, D., Baran, A. J., Boutle, I., Brooks, M., Earnshaw, P., Edwards, J., et al. (2019). The Met Office Unified Model Global Atmosphere 7.0/7.1 and JULES Global Land 7.0 configurations. *Geoscientific Model Development*, *12*(5), 1909–1963. https://doi.org/10.5194/gmd-12-1909-2019

Wang, W., Zender, C. S., van As, D., Smeets, P. C, & van den Broeke, M. R. (2016). A Retrospective, Iterative, Geometry-Based (RIGB) tilt-correction method for radiation observed by automatic weather stations on snow-covered surfaces: application to Greenland, *10*(2), 727–741. https://doi.org/10.5194/tc-10-727-2016

Wiesenekker, J., Kuipers Munneke, P., van den Broeke, M., & Smeets, C. J. P. P. (2018). A multidecadal analysis of Föhn winds over Larsen C ice shelf from a combination of observations and modeling. *Atmosphere*, *9*(5), 172.

Wille, J. D., Bromwich, D. H., Nigro, M. A., Cassano, J. J., Mateling, M., Lazzara, M. A., & Wang, S. H. (2016). Evaluation of the AMPS boundary layer simulations on the Ross Ice Shelf with tower observations. *Journal of Applied Meteorology and Climatology*, *55*(11), 2349–2367. https://doi.org/10.1175/JAMC-D-16-0032.1

Zängl, G. (2003). Deep and shallow south foehn in the region of Innsbruck: Typical features and semi-idelized numerical simulations. *Meteorology and Atmospheric Physics*, *83*(3), 237–261. https://doi.org/10.1007/s00703-002-0565-7

Zheng, F., Li, J., Clark, R. T., & Nnamchi, H. C. (2013). Simulation and projection of the Southern Hemisphere annular mode in CMIP5 models. *Journal of Climate*, *26*(24), 9860–9879. https://doi.org/10.1175/JCLI-D-13-00204.1